City Research Online

City, University of London Institutional Repository

Citation: Naseri, H., Koukouvinis, P., Malgarinos, I. & Gavaises, M. (2018). On viscoelastic cavitating flows: A numerical study. Physics of Fluids, 30(3), 33102. doi: 10.1063/1.5011978

This is the accepted version of the paper.

This version of the publication may differ from the final published version.

Permanent repository link: https://openaccess.city.ac.uk/id/eprint/19438/

Link to published version: https://doi.org/10.1063/1.5011978

Copyright: City Research Online aims to make research outputs of City, University of London available to a wider audience. Copyright and Moral Rights remain with the author(s) and/or copyright holders. URLs from City Research Online may be freely distributed and linked to.

Reuse: Copies of full items can be used for personal research or study, educational, or not-for-profit purposes without prior permission or charge. Provided that the authors, title and full bibliographic details are credited, a hyperlink and/or URL is given for the original metadata page and the content is not changed in any way.

City Research Online: http://openaccess.city.ac.uk/ publications@city.ac.uk

On viscoelastic cavitating flows: A numerical study

Homa Naseri, Phoevos Koukouvinis, Ilias Malgarinos and Manolis Gavaises

School of Mathematics, Computer Science & Engineering, City, University of London, London, Northampton Square, EC1V 0HB, UK

Keywords:

Cavitation, Viscoelasticity, Phan-Thien-Tanner Fluid

Abstract

The effect of viscoelasticity on turbulent cavitating flow inside a nozzle is simulated for Phan-Thien-Tanner (PTT) fluids. Two different flow configurations are used to show the effect of viscoelasticity on different cavitation mechanisms, namely cloud cavitation inside a step nozzle and string cavitation in an injector nozzle.

In incipient cavitation condition in the step nozzle, small-scale flow features including cavitating microvortices in the shear layer, are suppressed by viscoelasticity. Flow turbulence and mixing is weaker compared to the Newtonian fluid, resulting in suppression of microcavities shedding from the cavitation cloud. Moreover, mass flowrate fluctuations and cavity shedding frequency are reduced by the stabilizing effect of viscoelasticity. Time averaged values of the liquid volume fraction show that cavitation formation is strongly suppressed in the PTT viscoelastic fluid, and the cavity cloud is pushed away from the nozzle wall.

In the injector nozzle, a developed cloud cavity covers the nozzle top surface while a vortex-induced string cavity emerges from the turbulent flow inside the sac volume. Similar to the step nozzle case, viscoelasticity reduces the vapor volume fraction in the cloud region. However, formation of the streamwise string cavity is stimulated as turbulence is suppressed inside the sac volume and the nozzle orifice. Vortical perturbations in the vicinity of the vortex are damped allowing more vapor to develop in the string cavity region. The results indicate that the effect of viscoelasticity on cavitation depends on the alignment of the cavitating vortices with respect to the main flow direction.

1. Introduction

Cavitation dynamics and control is the subject of ongoing research with applications in pumps and propellers[1–3], injector nozzles[4–6] and medicine[7–9]. In nozzle flows, cavitation vapors block the effective flow passage area, significantly reducing the nozzle discharge coefficient[10–13]. Computational fluid dynamics (CFD) studies and X-rays of cavitating flows can directly show the reduction of fluid density in a nozzle due to cavitation [4,6,14–17]. Fully compressible simulations of cavitating nozzle flows can reveal that pressure waves produced during the bubble collapse events increase the jet instabilities and promote the primary jet breakup[17].

Fluid properties can affect the in-nozzle flow by modifying the flow turbulence and cavitation. This is because formation and collapse of cavitation vapors is subject to pressure fluctuations due to local flow instabilities and a two-way interaction exists between cavitation and turbulence. Moreover, collapse of cavitation bubbles is a primary mechanism for vorticity production and enhancement of streamwise velocity fluctuations[18–21]. Compression and expansion of cavitation vapors results in misalignment of the density gradients and the pressure gradients, hence the baroclinic torque (the source term $e_{ijk}\frac{\partial \rho}{\partial x_j}\frac{\partial p}{\partial x_k}/\rho^2$ appearing in the vorticity transport equation) is increased, producing vorticity [19,20]. Time-resolved X-ray densitometry of cavitation void-fraction in a cavity cloud[22] has identified that in addition to the re-entrant jet motion, bubbly shock propagation due to reduction of speed of sound in the mixture region, is responsible for the shedding of the cavitation cloud. More recently, high speed phase contrast imaging using synchrotron radiation has been used to provide details on the temporal evolution of cavitating vortices[23].

In addition to compressibility effects, cavitation also modifies the size and shape of the vortical structures in the flow and hence the interaction between the small and large

scales. Experimental analysis using PIV-LIF in a cavitating mixing layer has shown a reduction in the size of the coherent vortices as cavitation intensifies[21]. Turbulence anisotropy is increased as cavitation enhances the diffusivity in the streamwise direction while damping the cross-stream diffusivity [21]. Moreover, bubbles in vortex rings can distort and elongate an initially circular vortex core, as the bubble volume forces (pressure gradient, viscous and buoyancy forces) change the momentum in the liquid phase [24].

Compared to single-phase fluids, bubbly mixtures have different bulk properties such as viscosity, density and compressibility which modify the turbulent flow dynamics[25]. Injection of gas bubbles can provide lubrication for external liquid flows and a great body of research is dedicated to understanding the mechanism of drag reduction in bubbly flows [25–30]. The near-wall population of bubbles is an important factor for drag reduction, as the bubbles located in the buffer layer region can interact and modify the streamwise vortices [25]. Bubbles create a lift force in the wall-normal direction which disrupts the flux of energy from the large scales to the dissipative scales[27].

Viscosity and elasticity of bubbly mixtures contribute to the resistance of such mediums to deformation in fluid flow[31]. In fact bubbly liquids can be modelled using constitutive equations to describe their viscoelastic properties[32]. However, not much is known about the effect of viscoelasticity in turbulent cavitating flows and studies discussing viscoelastic properties in turbulent flows mainly focus on turbulent drag reduction.

Turbulent drag reduction by viscoelastic additives was first discovered by Toms [33] in 1948, since then it has been numerically and experimentally studied extensively[34–48]. Modification of fluid properties and flow turbulence is achieved even using very dilute solutions of high molecular weight polymers[49] or surfactant systems [50]. This knowledge is applied in oil delivery pipelines or district heating/cooling systems to reduce the turbulent drag, heat losses and the pumping costs [51,52].

The drag reduction mechanism in viscoelastic fluids is related to the interaction between the polymers and turbulence. Polymer viscosity as well as polymer elasticity, measured in terms of relaxation time, are both shown to be effective in this mechanism; however viscosity and elasticity effects form the basis for two theories describing drag reduction[43]. In the theory based on polymer viscosity, stretching of the polymers increases the total viscosity, suppressing the Reynolds stresses in the buffer layer region. As a result the thickness of the viscous sub-layer is increased and the turbulent drag is reduced [43,53–55]. In the elastic theory, the onset of drag reduction is when the elastic energy in the polymers becomes comparable to the Reynolds stresses in the buffer layer at length scales larger than the Kolmogorov scale. Consequently the energy cascade is truncated as the small-scales are suppressed and the viscous sublayer is thickened resulting in drag reduction [43,56].

Literature studies that correlate viscoelasticity and cavitation mainly focus on bubble dynamics in viscoelastic tissue-like medium. Microbubbles can act as ultrasound contrast agents[57] and bubble cluster collapse events can be used to destroy kidney stones (lithotripsy)[58] and malignant tissue (histotripsy)[58]. Viscoelasticity inhibits the high velocity liquid jet formed during the bubble collapse[59–63] and reduces the pressure amplitudes of acoustic emissions in ultrasound induced cavitation[61,64]. Viscous effects inhibit large bubble deformations and prevent incoherent bubble oscillations [62]. In a viscoelastic fluid, bubble oscillations can be damped by viscosity and compressibility effects, however at large elasticity values viscous damping becomes almost negligible and mainly compressibility effects are important[65]. When elasticity effects are small, viscous damping is more dominant but compressibility can also have a substantial contribution to the damping mechanism[65] and should be accounted for in strong collapse events[66].

Bubble oscillations are enhanced when the relaxation time of the viscoelastic media is increased[65–67]. At high relaxation times, bubble motion is more violent and less damped, resulting in higher bubble growth rates [66]. This is because when elasticity is high, the surrounding fluid behaves like an inviscid medium, whereas for low relaxation times (negligible elasticity) the behavior of the surrounding fluid is Newtonian [66].

Flow rotation and recirculation regions regularly appear in practical flow conditions where pre-existing bubbles and nuclei are convected into areas of low pressure. In swirling flow conditions, cavitation inception can happen in the low pressure core of large scale vortices forming in regions of high vorticity. This phase change mechanism is known as “vortex cavitation”[68] and it can appear in propellers, turbines and hydrofoils as well as inside the fuel injector nozzles where it is referred to as “string cavitation” [69,70]. Geometric constrictions such as sharp turns at a nozzle entrance[14] or a venturi throat[20], also generate flow instabilities that produce clouds of vapor. “Cloud cavitation” regions are characterized by a re-entrant jet motion and the periodic growth and shedding of the vapor clouds [71]. Injection of polymers can be effective in delaying the tip vortex cavitation in marine propellers [72] as the pressure fluctuations in the cavitation inception region are supressed[73]. However studies on interaction of viscoelasticity and cavitation are scarce in the literature.

This study aims to provide an understanding about the effect of viscoelasticity on cavitating flows and demonstrate some of the physical aspects of this type of flow. In particular, the effect of viscoelasticity on vapor production in cloud cavitation and string cavitation mechanisms in turbulent flow conditions is investigated in two different injector configurations. As it was discussed earlier, viscoelasticity can alter flow turbulence and bubble dynamics, hence cavitation inception and development are also expected to be altered in viscoelastic fluids due to the two-way interaction between cavitation and turbulence.

Numerical simulations of the Navier-Stokes equations are performed using the finite volume method for the flow through a step nozzle in incipient cavitation condition and in an injector nozzle that has both cloud cavitation and string cavitation structures. Instantaneous and time-averaged flow and cavitation structures demonstrate the differences between the inception and development of cavitation structures in Newtonian and viscoelastic fluids.

2. Numerical framework and setup

Flow turbulence can be most accurately described using direct numerical simulations (DNS), however this requires capturing the sharp interface between different phases and a grid size set to the smallest flow scales (Kolmogorov scale) which is not currently affordable. Alternatively, large eddy simulations (LES) can capture the large scale instabilities and vortical structures involved in inception and shedding of cavitation vapors and can be used for practical cases. The Phan-Thien-Tanner model [74] is used to model the viscoelastic fluid, which provides a constitutive equation taking into account the polymers microstructure. This model is based on a network theory and assumes that polymer junctions constantly break and reform, so unlike viscoelastic models that consider the polymers to act as elastic beads and spring dumbbells, the PTT polymer network has a dynamic nature. Moreover, the PTT model has also been used to predict the viscoelastic flow behavior in dilute polymer solutions [75,76].

To model the multiphase flow the mixture model is used which assumes a homogeneous two phase flow where the mixture density ρ_m is computed from the vapor volume fraction α:

$$\rho_m = \alpha\rho_v + (1-\alpha)\rho_l \quad (1)$$

where ρ_v *and* ρ_l are the vapor and the liquid densities respectively and the vapor volume fraction α is calculated from the cavitation model presented in equation (7).

The mass and momentum conservation equations for the mixture are:

$$\frac{\partial \rho_m}{\partial t} + \frac{\partial (\rho_m \mathbf{u}_i)}{\partial x_i} = 0 \tag{2}$$

$$\frac{\partial \rho_m \mathbf{u}_i}{\partial t} + \frac{\partial \left(\rho_m \mathbf{u}_i \mathbf{u}_j\right)}{\partial x_j} = -\frac{\partial p}{\partial x_i} + \frac{\partial}{\partial x_j}\left(\mu_{eff}\left(\frac{\partial \mathbf{u}_i}{\partial x_j} + \frac{\partial \mathbf{u}_j}{\partial x_i}\right)\right) + \frac{\partial \boldsymbol{\tau}_{ij}}{\partial x_i} \tag{3}$$

The last term in the momentum equation represents the source term from the viscoelastic stress contribution. μ_{eff} is the effective viscosity which is the molecular viscosity plus the turbulent viscosity.

Flow turbulence is modelled using the wall-adapting local eddy viscosity (WALE) model developed for wall-bounded flows[77] where the eddy viscosity is a function of both local strain rate and rotation rate:

$$\mu_t = \rho L_s^2 \frac{\left(\mathbf{S}_{ij}^d \mathbf{S}_{ij}^d\right)^{3/2}}{\left(\mathbf{S}_{ij}\mathbf{S}_{ij}\right)^{5/2} + \left(\mathbf{S}_{ij}^d \mathbf{S}_{ij}^d\right)^{5/4}} \tag{4}$$

The spatial operator $L_s = \min\left(d, C_w U^{1/3}\right)$ is defined based of the distance from the wall and C_w = 0.325, so the eddy viscosity predicts the correct y^3 near-wall asymptote and naturally goes to zero at the wall. $\mathbf{S}_{ij}$ is the strain rate tensor and $\mathbf{S}_{ij}^d$ is the deformation tensor:

$$\mathbf{S}_{ij} = \frac{1}{2}\left(\frac{\partial \mathbf{u}_i}{\partial x_j} + \frac{\partial \mathbf{u}_j}{\partial x_i}\right) \tag{5}$$

175 $$\mathbf{S}_{ij}^{d} = \frac{1}{2}\left[\left(\frac{\partial \mathbf{u}_i}{\partial x_j}\right)^2 + \left(\frac{\partial \mathbf{u}_j}{\partial x_i}\right)^2\right] - \frac{1}{3}\mathrm{tr}\left[\left(\frac{\partial \mathbf{u}_i}{\partial x_j}\right)^2\right]\delta_{ij} \quad (6)$$

176 And δ_{ij} is the Kronecker delta.

177 The cavitation model of Schnerr and Sauer [78] is employed which solves a transport
178 equation for the vapor volume fraction α using a mass transfer rate equation based on
179 the Rayleigh-Plesset equation for bubble dynamics:

180 $$\frac{\partial}{\partial t}(\alpha \rho_v) + \frac{\partial(\alpha \rho_v \mathbf{u}_i)}{\partial x_i} = \frac{\rho_v \rho_l}{\rho_m}\alpha(1-\alpha)\frac{3}{\Re_B}\left(\sqrt{\frac{2}{3}\frac{|p_V - p|}{\rho_l}}\right) sign(p_V - p) \quad (7)$$

181 p_V is the vapor pressure, p is the local pressure and $\Re_B$ is the bubble radius taken as
182 10^{-6} m which is a few orders of magnitude smaller than the cell size inside the nozzles.
183 Reducing the bubble radius too much will push the mass transfer rate to infinity as the
184 phase change process tends toward thermodynamic equilibrium, however this will also
185 destabilize the solution.

186 Prediction of cavitation using mass transfer rate models has been quantitatively
187 validated by the authors recently using X-ray micro-CT measurements of vapor volume
188 fraction[6] inside an orifice. By considering a mass transfer rate between the two phases,
189 the liquid/vapor mixture becomes compressible even if the pure phases are treated as
190 incompressible and the mass transfer rate is the dominant term affecting the sonic
191 velocity of the mixture[79]. Moreover, as the mass transfer rate tends to infinity the model
192 moves toward thermodynamic equilibrium and tends asymptotically to a barotropic
193 cavitation model.

194 The PTT constitutive model [74] assumes that the fluid element contains several polymer
195 junctions which can move by polymer extension and relaxation and the rate of “creation
196 and destruction” of the junctions is determined from the strain rate tensor:

197 $$\lambda \overset{\nabla}{\boldsymbol{\tau}}_{ij} + f(tr(\boldsymbol{\tau}_{ij})).\boldsymbol{\tau}_{ij} = \mu_p\left(\frac{\partial \mathbf{u}_i}{\partial x_j} + \frac{\partial \mathbf{u}_j}{\partial x_i}\right) \quad (8)$$

198 where $\boldsymbol{\tau}_{ij}$ is the viscoelastic stress, μ_p is the polymer viscosity and $f(tr(\boldsymbol{\tau}_{ij}))$ is:

199 $$f(tr(\boldsymbol{\tau}_{ij})) = 1 + \varepsilon \frac{\lambda}{\mu_p}(tr(\boldsymbol{\tau}_{ij})) \quad (9)$$

200 where λ is the polymer relaxation time and the extensibility factor ε is 0.02 for dilute
201 solutions[80]. For $\varepsilon \to 0$ the Oldroyd-B model is recovered and both of these models
202 have been widely used in the literature to fit the experimental data of viscoelastic fluids.

203 $\overset{\nabla}{\boldsymbol{\tau}}_{ij}$ is the Oldroyd upper convected derivative:

204 $$\overset{\nabla}{\boldsymbol{\tau}}_{ij} = \frac{\partial \boldsymbol{\tau}_{ij}}{\partial t} + \frac{\partial}{\partial x_k}(\mathbf{u}_k \boldsymbol{\tau}_{ij}) - \left(\boldsymbol{\tau}_{ik}\frac{\partial \mathbf{u}_j}{\partial x_k} + \boldsymbol{\tau}_{kj}\frac{\partial \mathbf{u}_i}{\partial x_k}\right) \quad (10)$$

205 The viscoelastic stress tensor has 9 components, however since the matrix is
206 symmetric, 6 transport equations are solved to get the full solution for $\boldsymbol{\tau}_{11}$, $\boldsymbol{\tau}_{12} = \boldsymbol{\tau}_{21}$,
207 $\boldsymbol{\tau}_{13} = \boldsymbol{\tau}_{31}$, $\boldsymbol{\tau}_{22}$, $\boldsymbol{\tau}_{23} = \boldsymbol{\tau}_{32}$ and $\boldsymbol{\tau}_{33}$. At the end of each iteration, the values of the
208 velocity gradient tensor are used to calculate the viscoelastic stress terms. The
209 viscoelastic stress source term (equation (3)) is then added to the momentum
210 equations in the subsequent iteration. Subgrid scale viscoelastic effects are neglected
211 in calculations since, to the best of our knowledge, no such models have been
212 developed for PTT fluids as this requires direct numerical simulation and experimental
213 data for validation.

214 A pressure based solver is employed to solve the differential equations using the
215 commercial code Fluent 17.0 with user defined functions for implementation of the
216 viscoelastic model and the results are post processed using the Tecplot software.

Temporal integration is performed using second order implicit backward discretization. Momentum equations are solved using gamma differencing scheme[81] and viscoelastic stress terms are discretized with first order upwind scheme. Moreover, an artificial diffusion term is added to the viscoelastic stress transport equations, such that the dimensionless artificial diffusivity ($D = k/u_\tau H$, where k is constant artificial diffusivity, u_τ is the friction velocity and H is the nozzle width) is kept below 0.1, this was necessary in order to achieve a stable solution by smoothing the sharp gradients in the viscoelastic stress terms [82]. The vapor volume fraction transport equation is discretized with the quadratic upstream interpolation for convective kinetics (QUICK) scheme to achieve an accurate representation of the high density ratio field.

Table I. Boundary conditions at inlet and outlet surfaces. Total pressure values are taken from the injection pressure and downstream pressure values reported in Table II

Boundary value	Boundary condition
Inlet and outlet pressure	Dirichlet static pressure: $p_{static} = p_{total} - 0.5\rho u_i u_i$
Inlet normal velocity	Neumann: $\frac{\partial u_1}{\partial x_1} = 0$
Inlet tangential velocity	Dirichlet: $u_2 = u_3 = 0$
Inlet and outlet viscoelastic stresses	Neumann: $\frac{\partial \boldsymbol{\tau}_{ij}}{\partial x_k} \mathbf{e}_i \otimes \mathbf{e}_j \otimes \mathbf{e}_k = 0$
Inlet vapor volume fraction	Dirichlet: $\alpha = 0$
Outlet velocity	Neumann: $\frac{\partial \mathbf{u}_i}{\partial x_j} \mathbf{e}_i \otimes \mathbf{e}_j = 0$
Outlet vapor volume fraction	Neumann for $u_i n_i > 0$: $\frac{\partial \alpha}{\partial x_i} = 0$ Dirichlet for $u_i n_i < 0$: $\alpha = 0$ (n is the normal vector)

In the step nozzle test case, pressure and velocity are linked using the pressure implicit with splitting of operator (PISO) algorithm which is based on a predictor-corrector approach. Initially, the momentum equation is solved using a guessed pressure field. A

231 pressure correction equation which is derived from the momentum and continuity
232 equations, is then used to correct the velocities[83].

233 In the injector test case, a coupled pressure based solver was used in order to achieve
234 a faster convergence rate compared to the aforementioned segregated solver. In the
235 coupled solver algorithm, the pressure and momentum are solved simultaneously and
236 the pressure corrector is used to update the velocities[84].

Table II. Operating conditions for the step nozzle and the injector nozzle simulations. Cavitation number is calculated from equation (11)

Test case	Injection pressure P_{in} (KPa)	Downstream pressure $P_{downstream}$ (KPa)	Saturation pressure P_v (KPa)	Cavitation number Cn
Step nozzle	238.2	101.3	2.3	1.38
Injector	182385	5066.2	130	35.9

237

238 The polymer relaxation times chosen in this study (reported in Table III) are in the range
239 measured for dilute viscoelastic solutions in low viscosity solvents[85]. The molecular
240 weight of the polymer used in the non-polar solution in the study are reported 6.9 g/mol
241 and 1.6 g/mol for the polymer in the aqueous solution and the concentration range
242 corresponding to the chosen relaxation times is ~ 0.1% wt. The relaxation times are
243 large compared to the flow time scales such as the turnover time of large and small
244 eddies so it is expected that they alter the flow topology. When polymer relaxation
245 times are comparable to flow time scales, the turbulent kinetic energy cascade can be
246 altered resulting in turbulent drag reduction[49,86].

247 To characterize the polymer viscosity, the viscosity ratio β is used ($\beta = \mu_s / \mu_0$), where
248 $\mu_0 = \mu_s + \mu_p$ is the total viscosity and μ_s and μ_p are the solvent and the polymer

viscosities. One of the main objectives of this study is to examine how viscoelasticity can affect the cavitation structures. For this purpose we conducted a preliminary study on the effect of the polymer viscosity and observed clear changes (instantaneous and time-averaged) in cavitation volume fraction when the viscosity of the polymer was large compared to the solvent viscosity. High polymer viscosity values (when β is as small as 0.2)[87] can damp the turbulent shear stress and contribute to reduction of the turbulent drag[87].

Table III. Fluid properties for the step nozzle and the injector nozzle simulations. *For Diesel liquid viscosity, the Kolev correlation in equation (14) is used, β value is then calculated from the average viscosity in the flow field.

Test case	Fluid	Liquid density ρ_l (Kg/m^3)	Vapor density ρ_v(Kg/m^3)	Liquid (solvent) viscosity μ_s (Pa.s)	Vapor viscosity μ_v (Pa.s)	Polymer viscosity μ_p (Pa.s)	Polymer relaxation time λ (s)
Step nozzle (Newtonian)	Water	998.16	1.71E-02	1.02E-03	9.75E-06	-	-
Step nozzle (Viscoelastic)	β =0.1	998.16	1.71E-02	1.02E-03	9.75E-06	9E-03	4E-02
Injector (Newtonian)	Diesel	747.65	6.56	Eq 14	7.50E-06	-	-
Injector (Viscoelastic)	β=0.1*	747.65	6.56	Eq 14	7.50E-06	2E-02	8E-03

2.1. Step nozzle test case

The geometry of the step nozzle is shown in Figure 1(a) which is based on an experimental study[88] designed to investigate cavitation in a rectangular injector. Cavitation development inside the nozzle from incipient condition to fully developed condition is visualized using high speed imaging, moreover laser doppler velocimetry (LDV) measurements of streamwise velocity and RMS of turbulent velocity are provided for incipient cavitation condition in water. These experimental data were

265 previously used to examine the performance of the turbulence model and the cavitation
266 model used in the current study [89]. The data is only available for water and to the best
267 of author's knowledge no studies in the literature provide similar data for viscoelastic
268 cavitating flows.

269 Cavitation starts to develop inside the nozzle as water is injected at 0.16 MPa into the
270 atmospheric pressure while the flowrate is 40 mL/s. The injection pressure is increased
271 and cavitation intensifies until fully developed cavitation conditions are reached at 0.31
272 MPa injection pressure and 62 mL/s flowrate.

273 A hemispherical outlet geometry is added to the domain with 14 mm diameter to allow
274 a uniform assignment of the outlet pressure boundary condition away from the nozzle
275 exit and boundary and operating conditions are reported in Table I and Table II.

276 In the simulation test case water flows through the nozzle with a flowrate of 48 mL/s,
277 the pressure difference across the nozzle is 1.38 bar while the injected liquid is
278 discharging into atmospheric pressure. The cavitation number (Cn defined in Equation
279 (11), $P_{injection}$, $P_{downstream}$ and P_v are the injection, downstream and vapor pressures
280 respectively) is 1.38 and the Reynolds number based on average liquid velocity in the
281 nozzle is 27700. These values are similar to those realized in real-size diesel injectors
282 operating at nominal injection pressures and correspond to the incipient cavitation
283 regime [88]:

284
$$Cn = \frac{P_{injection} - P_{downstream}}{P_{downstream} - P_v} \tag{11}$$

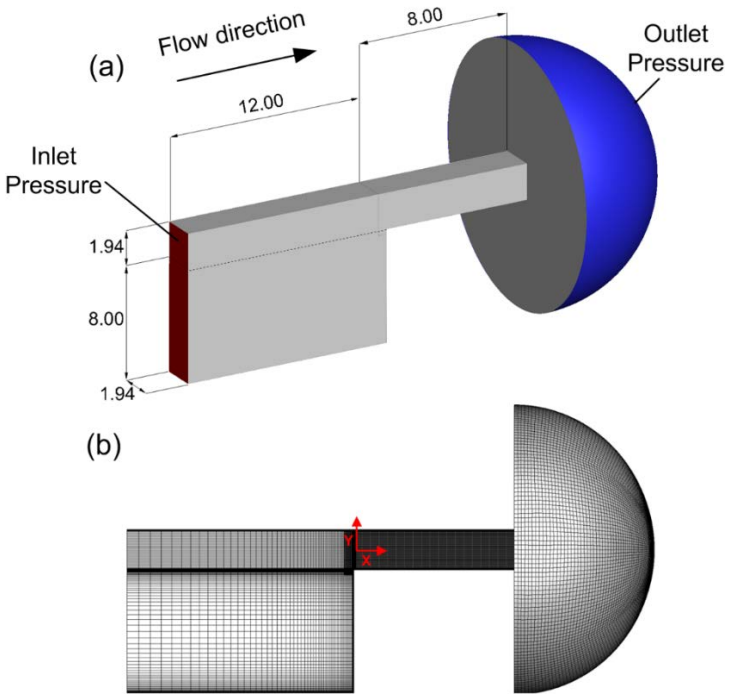

Figure 1. (a) Geometry of the step nozzle and the relevant dimensions in mm, inlet boundary (red color) and outlet boundary (blue color) surfaces are shown all the other surfaces are no–slip walls (grey color) (b)Computational grid with additional refinement inside the nozzle

The computational grid consists of unstructured hexahedral cells and additional refinement is used inside the constriction to achieve the cell size below the Taylor length scale λ_g (approximated from the characteristic length scale L = 1.94 mm and Reynolds number, $\lambda_g = (10/Re)^{0.5} L = 39$ μm). Estimation of Taylor microscale provides a guideline for grid resolution in practical LES studies[90,91]; by refining the mesh below this value the large scale turbulent eddies are captured as λ_g theoretically lies in the high wavenumber end of the inertial subrange. Taylor length scale characterizes the mean spatial extension of the velocity gradients[92,93] and is always much smaller than the integral scale (but not the smallest scale)[94]. The cell size inside the nozzle is 20 μm and it is refined to 2.5 μm near the walls, corresponding to y^+ values of 0.2-1. The time step corresponding to Courant-Friedrichs-Lewy (CFL) number of 0.5 is set to 1 μs in the Newtonian test case and for the viscoelastic case the time step is reduced to 0.5 μs for CFL of 0.25.

2.2. Injector nozzle test case

A common rail injector geometry section as shown in Figure 2 is simulated which has a more complex flow and cavitation mechanism compared to the step nozzle. This is a real-size Diesel fuel injector tip with five uniformly distributed holes and the nozzle holes are slightly tapered with a k factor of 1.1:

$$k = \frac{D_{in} - D_{out}}{10} \tag{12}$$

D_{in} and D_{out} are inlet an outlet dimeters of the hole measured in micrometers. The nozzle has an inlet and exit diameter of 0.37 mm 0.359 mm respectively and is 1.26 mm long. Nozzle hole tapering is linked to reduction of cloud cavitation but at the same time, formation of vortex or string cavities (presented in results section in Figure 10) inside the nozzle. By using taperd holes instead of cylindrical holes, string cavitation which forms inside large scale vortices entering the nozzle from the sac volume, can be intensified while cloud cavitation is reduced [70]. In this test case, the fuel passes through the needle passage before entering the sac volume (see Figure 2), where it recirculates as it enters the nozzle. A cavitation cloud forms at the top corner of the nozzle entrance due to the sharp turn in the flow streamline. Moreover, a large vortex enters the nozzle from the sac volume, with string cavitation forming in the core of this vortex inside the nozzle. A recent fully compressible implicit LES simulation of a 9-hole injector with needle motion[95] shows that elongated vortical structures which enter the nozzle from the sac volume and the overall flow features are present when compared to steady needle simulations at full needle lift.

The Reynolds number inside the nozzle and the sac volume reaches above 30,000 indicating the highly turbulent flow conditions of the injector. Considering the mesh resolution and the small time step required for simulating this case, the computational

cost of simulating the complete 5 hole geometry for Newtonian and viscoelastic fluids would be very high so 1/5th of the injector geometry (72˚) is simulated as shown in Figure 2 (b) and periodic boundary conditions are employed on the sides of the geometry.

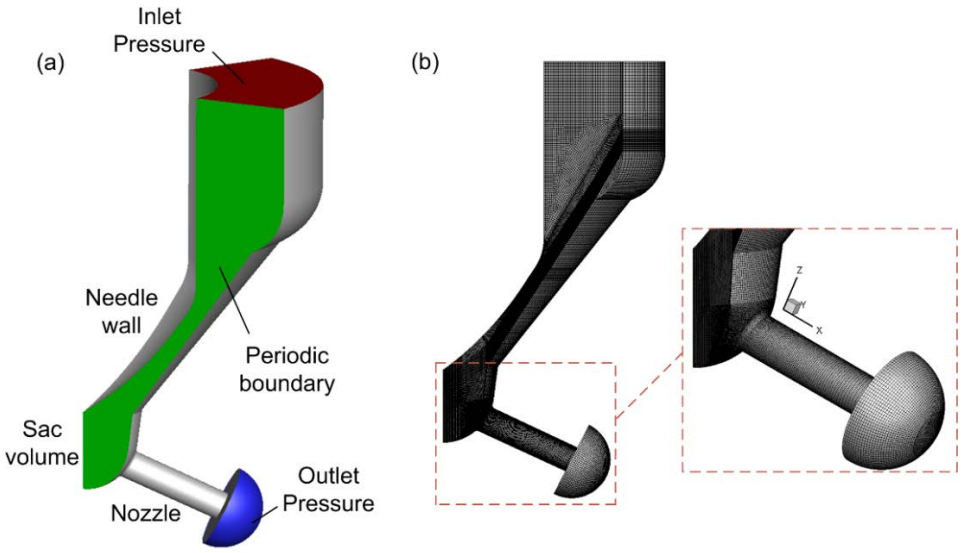

Figure 2. (a) Simulation domain for the injector test case. Boundary condition are indicated by colored surfaces; inlet and outlet boundaries are colored in red and blue respectively and the green surface shows the periodic boundary (another periodic boundary with the same cross section is located on the opposite side of the geometry), all the other surfaces are no–slip walls (grey color), (b) The computational grid for the injector, the domain is partitioned using blocking and it is hex-dominant except from an unstructured tetrahedral section in the sac volume

Inlet and outlet total pressures are fixed at $P_{injection}$ = 1800 bar and $P_{downstreamt}$ = 50 bar. Cavitation number for this condition is Cn =35.9, which is much higher than the step nozzle test case due to the higher pressure difference from the inlet to the outlet. In this condition fully developed cloud cavitation is located in the top surface of the nozzle, while the string cavity has a more intermittent appearance.

A hex-dominant block mesh is used for most parts of the geometry, except for a section in the sac volume upstream of the nozzle entrance, where unstructured tetrahedral mesh is used. The mesh resolution in the nozzle and the sac volume where cavitation develops is 7.5 µm with additional refinement near the walls. With this resolution, large scale flow structures, unsteady cavitation dynamics and vortex shedding can be

captured. The time step for the Newtonian flow condition is 5 ns for CFL of ~0.4 and for the viscoelastic case it is reduced to 2 ns and CFL of ~0.15.

The pressure levels inside the injector change significantly so the subsequent changes in the Diesel fuel properties are also considered. Hence the density and the viscosity of the fuel are calculated as a function of pressure. The density is calculated using Tait equation of state to represent the weak compressibility of the liquid Diesel:

$$p = B\left[\left(\frac{\rho}{\rho_{sat,L}}\right)^{n} - 1\right] + P_{sat} \tag{13}$$

where the bulk modulus B is 110 MPa, the material exponent n is 7.15 and $\rho_{sat,L}$ and P_{sat} are the liquid saturation density and saturation pressure respectively. The liquid viscosity is calculated based on the correlation proposed by Kolev[96] :

$$\log_{10}\left(\frac{10^{6}\mu_{L}}{\rho}\right) = 0.035065275 - \frac{0.000234373\ p}{10^{5}} \tag{14}$$

The values used for the fluid properties used in both test cases can be found in Table III.

3. Results and discussion

3.1. Step nozzle

As the flow detaches at the entrance of the nozzle (see Figure 3) a shear layer is formed between the flow passing through the nozzle and the recirculation region. Cavitation vapors appear in the core of microvortices in the shear layer and they are detaching and shedding from the cavity cloud in a cyclic manner. Contours of velocity magnitude in the mid-plane of the nozzle for the Newtonian and the viscoelastic fluids are presented in Figure 3. It is evident that the flowfield in the viscoelastic fluid appears

to have a more homogenous gradient. The black iso-lines show the areas where the pressure drops below the vapor pressure, i.e. the regions of cavitation inception. The cavitation inception regions appear more frequently in the Newtonian fluid and they cover a larger area of the nozzle's cross sectional area, indicating that more vapor is being produced in this fluid. It is likewise reported in the literature that the minimum pressure at a cavitation inception point (the core of a vortex developing in the wake of a cylinder) increases as the vorticity is reduced by viscoelasticity [97].

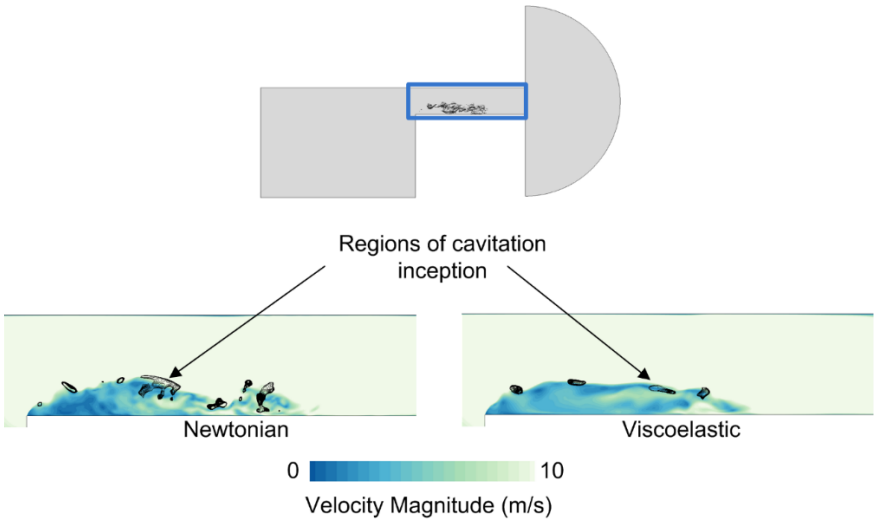

Figure 3. Nozzle geometry and cavitation in the shear layer (top), contours of the velocity magnitude for the Newtonian and the viscoelastic fluid in the mid-plane of the nozzle, the black iso-lines show regions with pressures below the vapor pressure (bottom)

The structure of the vortical features in the flow is shown in Figure 4 by means of the second invariant of the velocity gradient tensor[98] calculated from $II_A = -\frac{1}{2}\frac{\partial \mathbf{u}_i}{\partial x_j}\frac{\partial \mathbf{u}_j}{\partial x_i}$.

Spanwise Kelvin-Helmholtz-like vortices form right after the nozzle inlet as shown in Figure 4 (a), it can be clearly seen that significantly fewer vortices appear in the viscoelastic fluid. Inhibition of shear instability by polymer injection has previously been reported in the literature [99]. The 'polymer torque', which is the contribution of the viscoelastic stress to the vorticity evolution, increases the flow resistance to rotational motion and can inhibit the vortex sheet roll-up[97].

Further downstream, the vortex sheet breaks down, developing a range of small-scale and large-scale structures. It is evident that in the viscoelastic fluid spanwise vortices are inhibited while longitudinal vortices become more dominant. Enhancement of large scale coherent structures in the mixing layer is due to hindering of development of perturbations and a stronger vorticity diffusion in viscoelastic fluids[100]. This results in slower rotational motion of the neighboring vortices and delay of vortex pairing and merging, therefore the lifetime and the scale of the coherent structures is increased.

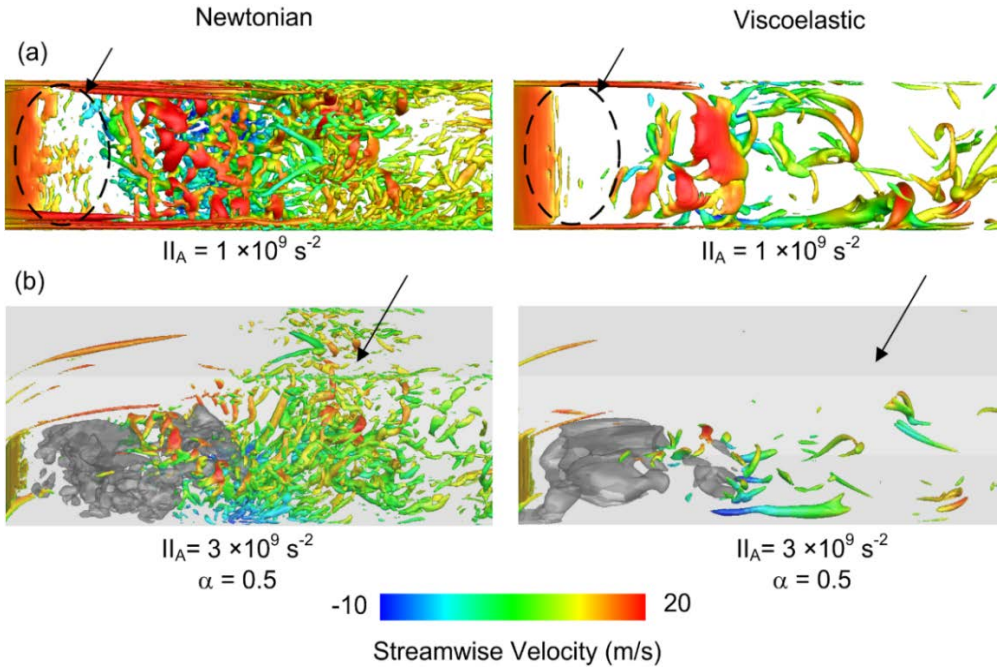

Figure 4. (a) Iso-surface of the second invariant of the velocity gradient with the value $1 \times 10^9\ s^{-2}$ colored with the streamwise velocity, image shown from the top (–Y) direction (b) 3D view of the iso-surface of the second invariant of the velocity gradient at $3 \times 10^9\ s^{-2}$ colored with the streamwise velocity along with iso-surface of 50% vapor volume fraction (grey color)

In Figure 4 (b) the iso-surface of 50% vapor volume fraction is presented along with the II_A iso-surface. After the collapse of the cavity cloud in the Newtonian fluid, a strong mixing region forms inside the nozzle. In the viscoelastic fluid however, the mixing is weaker and mainly vortices with larger diameters are forming as local instabilities are suppressed and vortical sub-structures are damped. Likewise enlargement of streamwise vortical structures and their elongation in the streamwise direction is

reported in turbulent channel flows [101]. This is due to tendency of polymers to strongly align in the streamwise direction, partially suppressing wall-normal and spanwise velocity fluctuations[102]. Moreover, the polymer viscosity resists the extensional deformation imposed by the motion of turbulent eddies[103,104].

The turbulence kinetic energy spectrum for the Newtonian and the viscoelastic fluid is shown in *Figure 5*, where k is the wave number and E(k) is the amplitude of the kinetic energy FFT calculated inside the nozzle. The graph represents the spatial spectrum of the turbulence kinetic energy, where $k = 2\pi n/L$ and n and L are the incremental spatial frequency number and the wavelength respectively.

Energy content of the low wavenumber scales is higher by ~15% in the Newtonian fluid, however the decay slope is also slightly faster (-5/3 in the Newtonian fluid in competition with ~-4/3 in the viscoelastic fluid) so the flow energy mainly contained within the inertial subrange eddies is similar in both cases.

At higher wavenumbers the difference becomes more evident as the Newtonian fluid has ~38% higher turbulence kinetic energy content, indicating that the small-scales in this fluid are more pronounced. This observation is expected as the small-scales are suppressed in the viscoelastic fluid as seen in Figure 4. This is consistent with experimental measurements of power spectra in wall-bounded polymeric flows which show that viscoelasticity can suppress turbulence kinetic energy at small-scales while having a negligible effect on large scales[105]. Moreover, in viscoelastic fluids, the kinetic energy removed from the large scales is partially dissipated by small-scales and partially converted into elastic energy which is then transferred back into the large scales. This will alter the nature of energy cascade usually seen in Newtonian fluids and reduce the energy content at the small-scales[106].

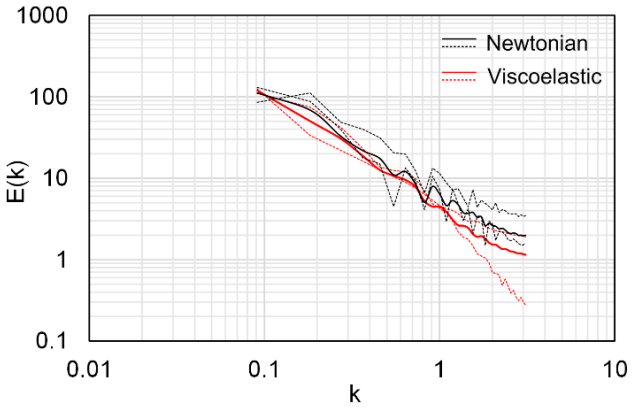

Figure 5. Energy spectra inside the step nozzle for the Newtonian and the viscoelastic fluid, dashed lines (----- and -----) show indicative examples of the spectra and continuous lines (—— and ——) show the mean value of the spectra for the Newtonian and viscoelastic fluid

In *Figure 6* (a) the development of the streamwise velocity component in the mid-plane of the nozzle presented. The magnitude of the negative velocity in the recirculation region ($-0.94 \leq Y \leq -0.4$) is larger in the Newtonian fluid on average by ~28% at X = 2mm and ~41% at X = 4 mm. The re-entrant jet velocity is responsible for detachment and shedding of the cavity cloud [71], therefore larger velocities in the recirculation region of the Newtonian fluid are indicative of a faster shedding process in this fluid.

In Figure 6 (b), the RMS of streamwise velocity which indicates the turbulent velocity, is plotted along the nozzle. Overall the weighted average of RMS of streamwise velocity over the computational cell volume inside the nozzle ($0 \text{ mm} < X < 8 \text{ mm}$) is reduced by 11% in the viscoelastic fluid. In Figure 6 (b), this effect is mainly visible in the lower half of the nozzle ($-0.94 \text{ mm} \leq Y \leq 0 \text{ mm}$), corresponding to the shear layer and flow recirculation regions. The effect of viscoelasticity on velocity fluctuations is more evident in Figure 6 (c) which shows the RMS of wall-normal velocity along the nozzle. Suppression of velocity fluctuations is stronger in the wall-normal direction compared to the streamwise direction and overall the RMS of wall-normal velocity is reduced by 27.5% inside the nozzle for the viscoelastic fluid. By suppressing the wall-normal

449 velocity fluctuations, polymers can more effectively reduce the turbulence generation

450 by vortices.

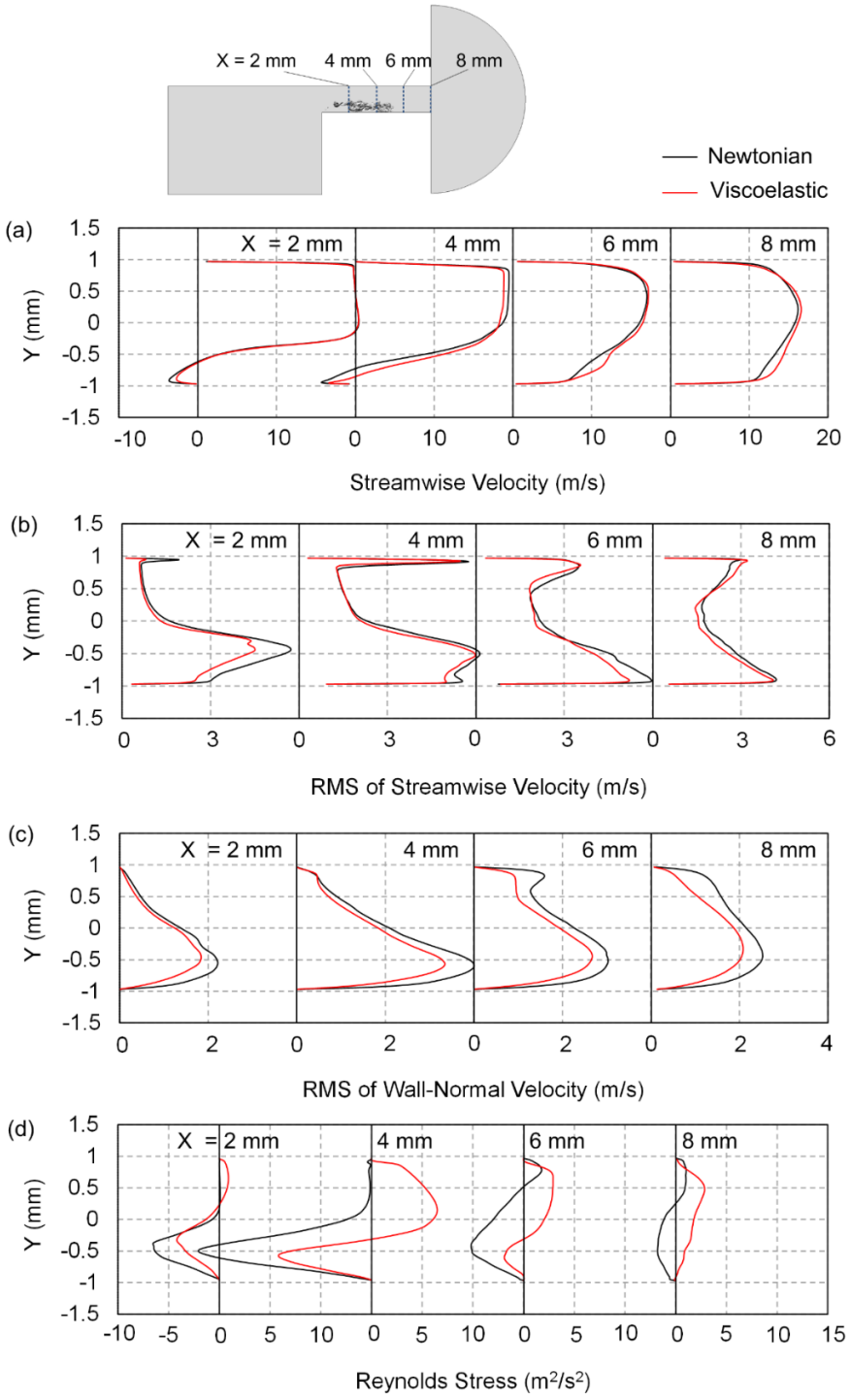

451

452 *Figure 6.Comparison of time-averaged values of the streamwise velocity, RMS of streamwise*
453 *velocity, RMS of wall-normal velocity and Reynolds stress ($-\overline{u'v'}$) in the Newtonian and the*
454 *viscoelastic fluid, data are presented in the mid-plane of the step nozzle at four different X*
455 *locations along the nozzle*

In Figure 6 (d) the Reynolds stress in the XY plane ($-\overline{u'v'}$) is plotted along the nozzle, positive and negative values of the Reynolds stress correspond to turbulence suppression and production respectively[107]. Negative values of Reynolds stress are produced by ejection and sweep motions which contribute to positive turbulence production and in general increase drag. Positive Reynolds stress values correspond to turbulence suppression and their increase generally results in drag reduction [107]. It is evident that in the recirculation region (-0.94 mm ≤ Y ≤ 0 mm) the Newtonian fluid has about twice the amount of Reynolds stress generated in the viscoelastic fluid, resulting in a higher level of turbulence generated in this region. In the bulk of the flow outside the recirculation zone, Reynold stresses have a positive value with a higher magnitude in the viscoelastic fluid indicating a stronger turbulence damping. Overall, stronger turbulence damping and lower turbulence levels generated in the viscoelastic fluid as seen in Figure 6 (b)-(d), can contribute to turbulence drag reduction and the mass flowrate is increased by~2%.

In *Figure 7* the development of cavitation inside the nozzle for the Newtonian and the viscoelastic fluid is compared in terms of 25% vapor volume fraction iso-surface. Cavitation is initiated in the core of microvortices forming in the shear layer and it grows as larger eddies form after the vortex sheet breakdown. Following, they form a cavity cloud which detaches due to the re-entrant jet motion and is convected toward the nozzle exit.

In the Newtonian fluid, small cavitation structures can be observed (red circle 1) with microcavities of various sizes (approximate diameter range of 30 μm-200 μm) shedding from the cloud, however such structures are not present in the viscoelastic fluid.

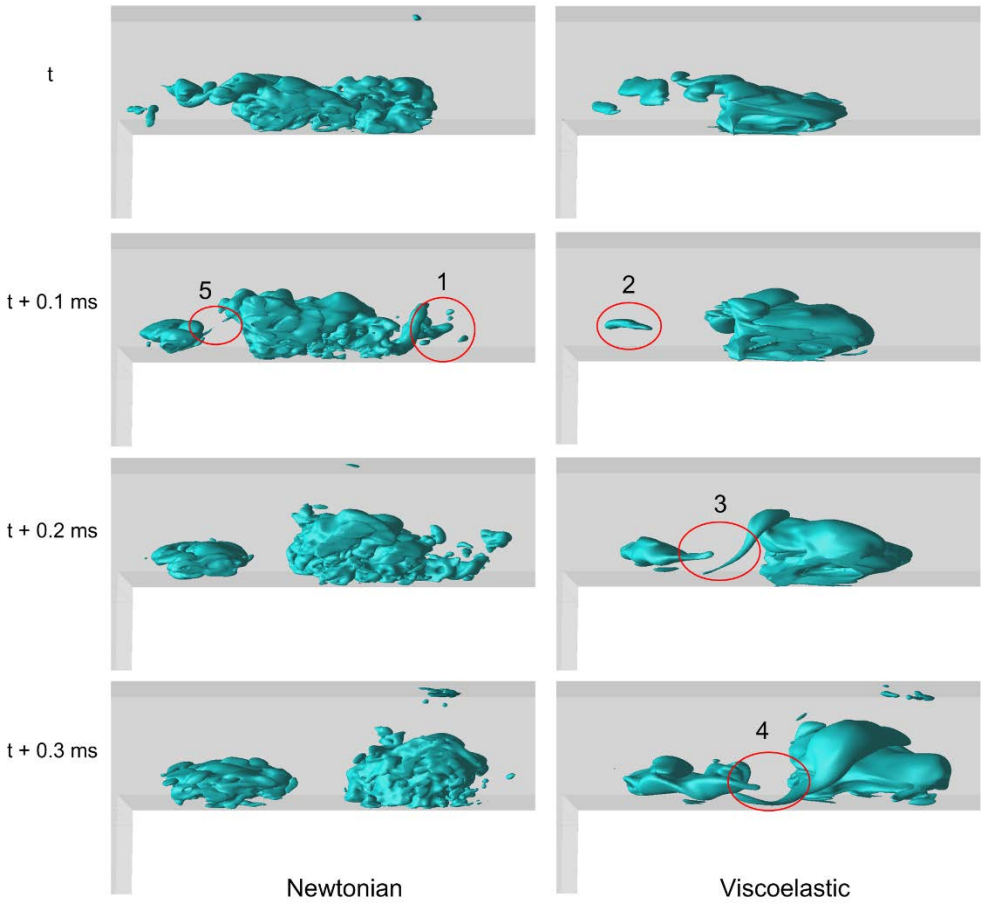

Figure 7.Cavitation development inside the step nozzle presented by means of 25% vapor volume fraction iso-surfaces, data are presented every 0.1 ms. Small microcavities shedding from the cloud (red circle 1) are not present in the viscoelastic fluid, cavitation vapors can initially shrink before growing (red circle 2) and larger streamwise vortices appear between the detached cloud and shear layer cavitation structures (red circle 3, 4 and 5)

The growth of the shear layer cavitating microvortices is rather faster in the Newtonian fluid; in the viscoelastic fluid it appears that the cavity initially shrinks (red circle 2) before growing. This can be due to the action of viscoelastic force resisting the fast deformation by liquid evaporation. Furthermore, cavitation structures in the viscoelastic fluid have an elongated shape. Larger streamwise cavitating vortices appear between the shear layer cavities and the detached cloud compared to the Newtonian fluid (see red circles 3, 4 and 5).

Due to the cyclic enlargement and shrinkage of the flow recirculation zone and the subsequent detachment and shedding of the cavitation vapors, the mass flowrate in the

nozzle also fluctuates in a cyclic manner. The fast Fourier transform (FFT) of mass flow rate time-evolution at nozzle outlet are presented in Figure 8 to indicate the dominant frequencies of the mass flowrate fluctuations. The dominant frequency in the Newtonian fluid is f = 168 Hz whereas in the viscoelastic fluid this values is reduced to f = 57 Hz, while the peak amplitude is increased by 42%. First and second harmonics of the dominant frequency can also be identified for both fluids at ~ 2f (343 Hz for the Newtonian fluid and 110 Hz for the viscoelastic fluid) and ~3f (524 Hz for the Newtonian fluid and 169 Hz for the viscoelastic fluid). Second harmonics with about double the dominant frequency are reported in pressure signals past a cavitating converging-diverging nozzle[108] and in the wake of a rectangular cavitating obstacle[109].

The reduction of the cavity shedding frequency can be due to the resistance of the viscoelastic fluid to development of vortical structures and therefore suppression of cavity growth in the core of vortices. Moreover, development of the cavitation cloud can be delayed as the cavity volume can shrink before growing in the viscoelastic fluid due to memory effects produced by fluid elasticity. In fact it was observed that some of the shedding events are completely suppressed while vapor builds-up in the cloud region. Therefore the subsequent shedding event is more violent in the viscoelastic fluid, thus while the dominant frequency is reduced its peak amplitude is higher.

Unlike the Newtonian fluid, at frequencies above ~400Hz there are effectively no fluctuations in the viscoelastic fluid, indicating that the viscoelastic fluid damps out the high frequency fluctuations. As the small-scale microcavities shedding from the cavitation cloud are suppressed (Figure 7), the subsequent velocity fluctuations due to growth, collapse and oscillations of these cavities can also be inhibited, resulting in damping of high frequency fluctuations.

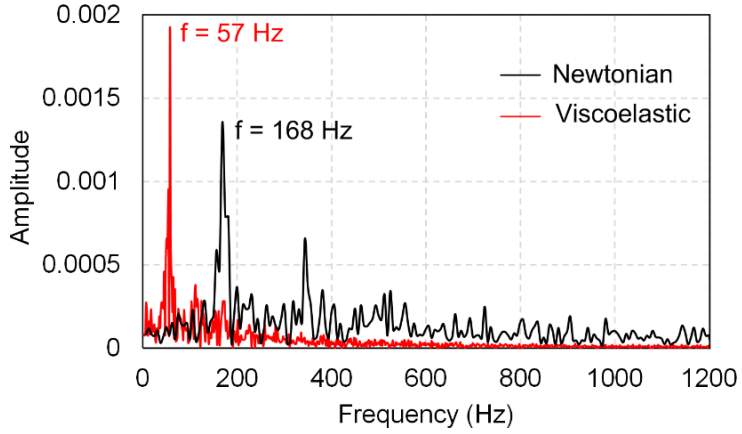

519

520 *Figure 8. FFT of mass flowrate fluctuations at the outlet of the step nozzle for the Newtonian*
521 *and the viscoelastic fluid, the dominant frequency corresponds to frequency of mass flowrate*
522 *fluctuations induced by cyclic growth and shedding of large cavity clouds*

523 The Strouhal number for vapor cloud shedding (St_v) based on the mass flowrate
524 fluctuation frequency (f), the cavity length (L_v) and the average streamwise velocity in
525 the cavity region (U_v) is defined as:

526 $$St_v = \frac{fL_v}{U_v} \quad (15)$$

527 For the Newtonian case the Strouhal number based on the dominant frequency is 0.22
528 and in the viscoelastic fluid the Strouhal number is reduced to 0.08. For Newtonian
529 fluids, a characteristic Strouhal number of 0.2 has been identified for cavitation cloud
530 shedding in a diverging step[71]. The detachment and shedding of the cavitation cloud is
531 partially driven by the re-entrant jet mechanism and the Strouhal number is
532 proportional to the re-entrant jet velocity [71], hence longer shedding periods can be due
533 to reduction of the re-entrant jet velocity. Observations regarding the reduction of
534 Strouhal number by viscoelasticity due to prolonged oscillation times has been reported
535 for vortex shedding past an obstacle [110–112].

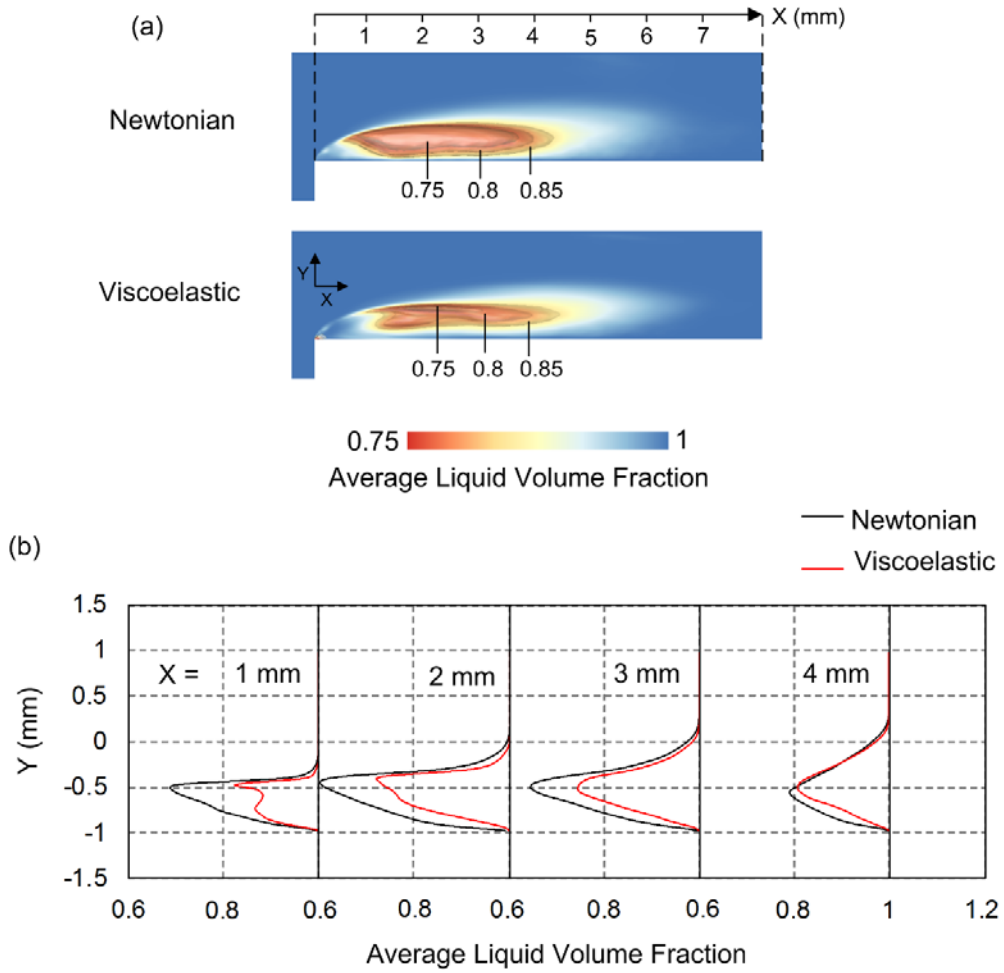

Figure 9. (a) Average liquid volume fraction (1-α) in the step nozzle mid-plane along with iso-surfaces of 75%, 80% and 85% average liquid volume fraction in the Newtonian and the viscoelastic fluid, (b) Average liquid volume fraction (1-α) inside the cavitation region for the Newtonian and the viscoelastic fluid, values taken along 4 lines passing through the cavitation cloud in the nozzle mid-plane

Finally, the time-averaged effect of viscoelasticity on the cavitation field is presented in Figure 9 by comparing the average liquid volume fraction inside the nozzle. It can be seen from Figure 9 (a) that the cavitation inception point is shifted further downstream the nozzle entrance; so vapor mainly starts to form at X ≈ 0.3 mm in the Newtonian fluid and at X ≈ 0.8 mm in the viscoelastic fluid. Moreover the thickness of the cavity cloud in this region is reduced from ~0.69 mm in the Newtonian fluid to ~0.58 mm in the viscoelastic fluid (~16% reduction).

In Figure 9 (b) values of the liquid volume fraction in four locations inside the cavitation cloud are compared. In all these locations the liquid volume fraction in the viscoelastic fluid is constantly higher. The average vapor volume fraction in the viscoelastic fluid integrated over the volume of the nozzle (0 mm < X < 8 mm) is reduced by 51%. Moreover it is evident that the cavitation suppression effect is stronger at the lower half of the cavity cloud -0.94 mm ≤ Y ≤ -0.5 mm (closer to the nozzle wall). Reduction of near wall vorticity fluctuations inhibits the near-wall eddies in viscoelastic fluids[113] which can be responsible for production and transport of cavitation vapors in this region.

3.2. Injector nozzle

In the injector nozzle, two distinct regions for cloud cavitation and string cavitation can be identified. Characteristics of different cavitation mechanisms in injector nozzles is described in the literature [70,114,115]. The cloud cavitation forms in a similar manner to the cavitation in the step nozzle; as the fluid enters the nozzle it takes a sharp turn at the entrance forming a fully developed vapor cloud which is mainly attached to the top surface of the nozzle and grows and sheds in a cyclic manner. The string cavitation forms in the high vorticity core of a large vortex entering the nozzle from the sac volume and it is located in the vicinity of the nozzle center (the streamlines and vectors forming the string cavitation are presented in Figure 10 (a)).

The local pressure drops from 100 MPa in the sac volume to 0.1 MPa (below the saturation pressure) inside the nozzle as the string cavity starts to form. The string cavity has an intermittent appearance as it can distort, break-up and elongate inside the nozzle, however in the viscoelastic fluid a larger and more stable vaporous core appears and time averaged values of vapor volume fraction will be used to further investigate this matter.

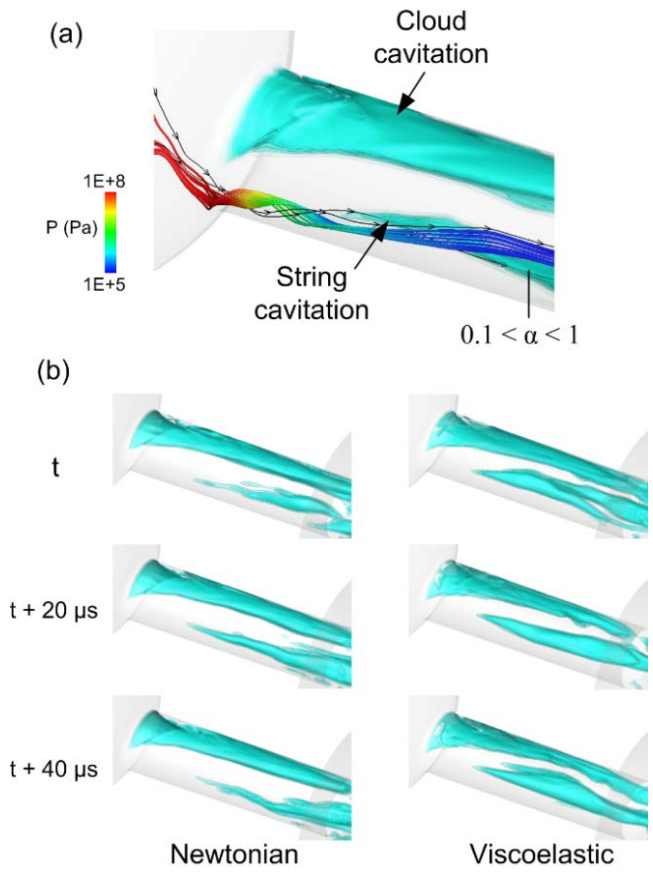

Figure 10. (a) Two distinct cavitation regions forming inside the injector nozzle, cavitation vapors are presented using 5 translucent vapor volume fraction iso-surfaces ranging from 0.1 to 1, the cavitating vortex can be seen entering the nozzle from the sac volume, the vortex is presented by streamlines colored with pressure (b) Indicative cavitation structures inside the nozzle at 20 μs intervals for the Newtonian and the viscoelastic fluid (0.1< α <1) showing a larger string cavity in the viscoelastic fluid.

Since the cloud cavitation and the string cavitation occur at different locations inside the nozzle, it is possible to examine the effect of viscoelasticity on each cavitation mechanism by geometrically separating the cavitation vapor volumes as seen in Figure 11 (a), which shows the separated cloud and the string cavitation structures in the same time step. The time-averaged vapor volume fraction data are separated into a cloud region and a string region by splitting the cross section of the nozzle into a top section (cloud, Y>35 μm) and a bottom section (string, Y<35 μm) using a plane along the nozzle axis. The vapor volume fraction in the string and the cloud region is

590 calculated in slices along the nozzle and the area weighted average value is used to
591 get the total vapor volume fraction. Vapor structures in the cloud and the string region
592 marginally intersect inside the nozzle but in the vicinity of the nozzle exit this overlap
593 can contribute to ~20% variations in the average vapor volume fraction in each region.
594 The overlapping regions are identified to be located in the area approximately ±40μm
595 from the nozzle axis and are displayed in the graph as error bars.

596 The time-averaged value of the total vapor volume fraction inside the nozzle is plotted
597 for the Newtonian and the viscoelastic fluid in Figure 11 (b). It is evident that the in-
598 nozzle cavitation mechanism is mainly due to cloud cavitation in the Newtonian fluid
599 and overall the vapor volume fraction in the Newtonian fluid is higher by 44%. Initially,
600 cavitation develops at the nozzle entrance due to the cloud cavitation mechanism,
601 increasing the vapor volume fraction in the nozzle up to ~0.16 in the Newtonian fluid
602 and up to ~0.08 in the viscoelastic fluid until X ≈ 0.4 mm. After this point cloud
603 cavitation declines and string cavitation starts to develop while reaching the nozzle exit.
604 In the viscoelastic fluid the vapor volume fraction of the cloud cavitation is higher than
605 string cavitation up to X ≈ 0.9 mm (70% into the nozzle length), and after this location
606 the string cavitation becomes more dominant. In the Newtonian fluid the rate of
607 reduction of the cloud cavity is ~17% faster than the rate of formation of string cavity,
608 hence the total vapor volume fraction is reduced after X ≈ 0.4 mm. Whereas in the
609 viscoelastic fluid, the string cavitation forms more abruptly at a rate ~46% faster than
610 the decline of the cloud cavity, hence the total vapor volume fraction increases steadily
611 up to X ≈ 1 mm, after this point vapor volume fraction is reduced as string cavitation
612 growth declines.

613 The main observation from comparing the changes in the vapor volume fraction in
614 different mechanisms is that viscoelasticity reduces cavitation formation in the cloud
615 cavitation region while increasing the string cavitation. This indicates that the strength

of the cavitating vortex in the nozzle core is increased in the viscoelastic fluid which can be related to the alignment of the cavitating vortex with respect to the main flow direction. The string cavitation is forming in the core of the quasi-streamwise vortex in the center of the nozzle, whereas the cloud cavitation vortices can have large radial velocity components which are expected to be inhibited by viscoelasticity.

In the core of vortices the angle between the velocity vector (U) and the vorticity vector (ω) tends to zero as the vectors become aligned, hence the normalized helicity (H_n), which is effectively the cosine of this angle, tends towards unity [116]:

$$H_n = \frac{U.\omega}{|U||\omega|} \tag{16}$$

The normalized helicity contours are plotted in Figure 11(c) in several locations inside the nozzle along with black isolines of $H_n = 0.95$. It is evident that in the viscoelastic fluid, the string cavitation core covers a larger area, whereas in the Newtonian fluid a smaller vortex core can be identified. In the step nozzle test case presented in the previous section, it is reported that the streamwise vortices become more dominant by viscoelasticity as the smaller scale vortices are damped. In wall-bounded viscoelastic flows[117,118] it is reported that streamwise vortices can become elongated and larger as wall-normal fluctuations are damped. It is argued that suppression of cross-stream fluctuations can further inhibit their auto-generation and therefore increase the lifetime and strength of the longitudinal vortices. Likewise in this case, suppression of small-scale eddies inside the injector nozzle can be responsible for stabilizing the local turbulence in the vicinity of the string cavity, allowing the development of a larger streamwise vortex and delaying the vortex breakdown, which in turn can result in higher amounts of vapor to be produced in the vortex core.

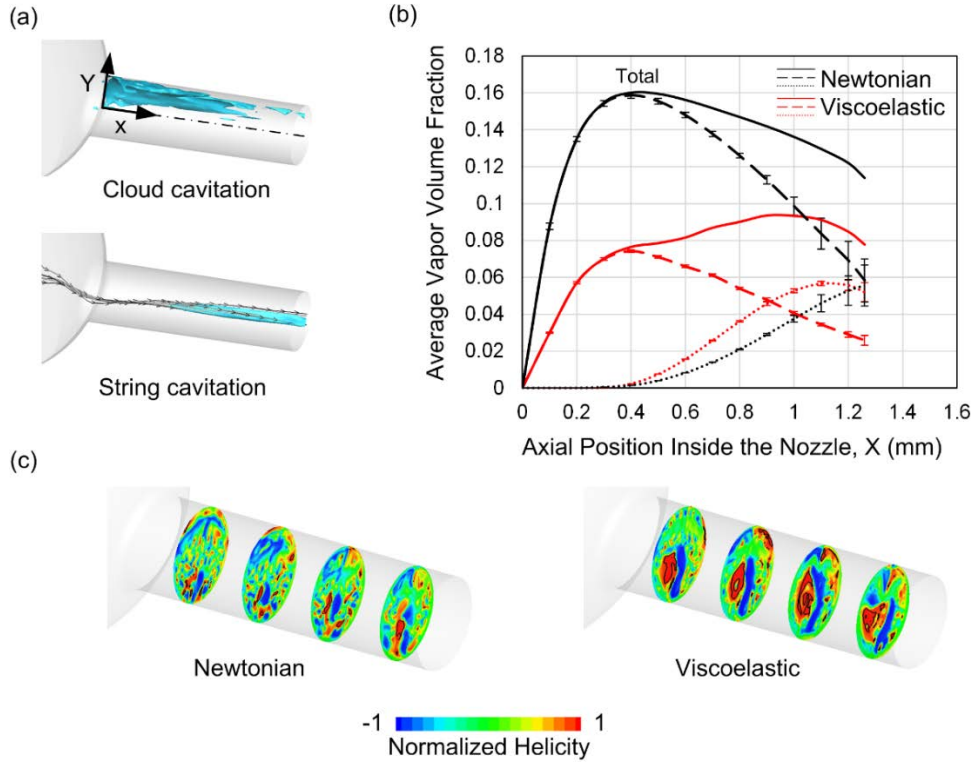

639

640 *Figure 11. (a) Separated vapor volume fraction regions inside the injector nozzle showing the*
641 *cloud cavitation and the string cavitation in term of iso-surfaces of 80% vapor volume fraction,*
642 *(b) Development of the string cavitation (dotted lines..... and .....), the cloud cavitation (dashed*
643 *lines ─ ─ and ─ ─) and the total vapor volume fraction (continuous lines ──and──) inside the*
644 *injector nozzle for the Newtonian and the viscoelastic fluid calculated in slices along the nozzle*
645 *axis using area weighted averages, error bars indicate the overlap of the vapor volume fraction*
646 *in the string and cloud the region in ±40μm in the vicinity of the nozzle axis,(c) Normalized*
647 *helicity (H_n) contours in slices inside the injector nozzle (at X = 0.2 mm, 0.5 mm, 0.8 mm and 1.1*
648 *mm), the black isolines show the regions of H_n = 0.95 and $H_n \rightarrow 1$ in vortex cores*

649 In the cavitation model of Schnerr and Sauer [78] in equation (7), the vapor volume
650 fraction equation source term describes the mass transfer rate (R) between the two
651 phases, so the positive values of R represent the evaporation rate and the negative
652 values are the condensation rate:

653
$$R = \frac{\rho_v \rho_l}{\rho_m} \alpha(1-\alpha) \frac{3}{\Re_B} \left(\sqrt{\frac{2}{3} \frac{|p_V - p|}{\rho_l}} \right) sign(p_V - p) \qquad (17)$$

654 In Figure 12 (a) and (b) the phase change rates in the cloud cavitation and the string
655 cavitation region at one instance are compared. The mass transfer rates are higher in
656 the cloud cavitation region, reaching 15×10^6 Kg/m^3.s as opposed to 0.5×10^6 Kg/m^3.s

657 in the string region of the Newtonian fluid, subsequently cloud cavitation is the main
658 mechanism of vapor production as it was seen in Figure 11 (b). In the cloud cavitation
659 graph, mass transfer starts at the X = 0 mm as the fluid enters the nozzle and peaks at
660 X ≈ 0.25 mm, however the string cavitation starts effectively at X > 0.2 mm in the
661 viscoelastic fluid and X >0.4 mm in the Newtonian fluid. The evaporation and
662 condensation rates in the cloud region are reduced in the viscoelastic fluid by ~2 orders
663 of magnitude, resulting in reduction of the vapor volume fraction in this region. However
664 in the string cavitation region this trend is reversed, i.e. evaporation rate is ~9 times
665 higher and condensation rate is ~2.5 times higher in the viscoelastic fluid.

666 The difference in the effect of viscoelasticity on cloud and string cavitation regimes can
667 be linked to the alignment of the vortical structures in each region with respect to the
668 direction of the main flow. The vortex cores identified in terms of the second invariant of
669 the velocity gradient are presented in Figure 12 (c). It is evident that viscoelasticity
670 does not affect the cloud and string vortical structures in the same manner. The vortex
671 which forms the string cavitation in the vicinity of the nozzle center (see arrow 1), is
672 enlarged by viscoelasticity while the vortical structures formed at the nozzle entrance in
673 the cloud region (see arrow 2) are strongly suppressed and only remnants of the
674 vortices are visible in the viscoelastic fluid. In the cloud cavitation region, vortices form
675 in the shear layer between the recirculating flow and the main flow, therefore they can
676 have large radial velocity components as the vorticity vector is likely to be located in the
677 cross-sectional plane of the nozzle (i.e. vortices rotating out of the cross sectional
678 plane). However in the string region the cavitating vortex is positioned in the
679 streamwise direction (vorticity vector in the axial direction). Therefore, as the polymers
680 tend to align with the main flow direction[102] and suppress the cross flow fluctuations[87],
681 viscoelasticity tends to damp the vortices in the cloud region while stimulating the string
682 cavity vortex.

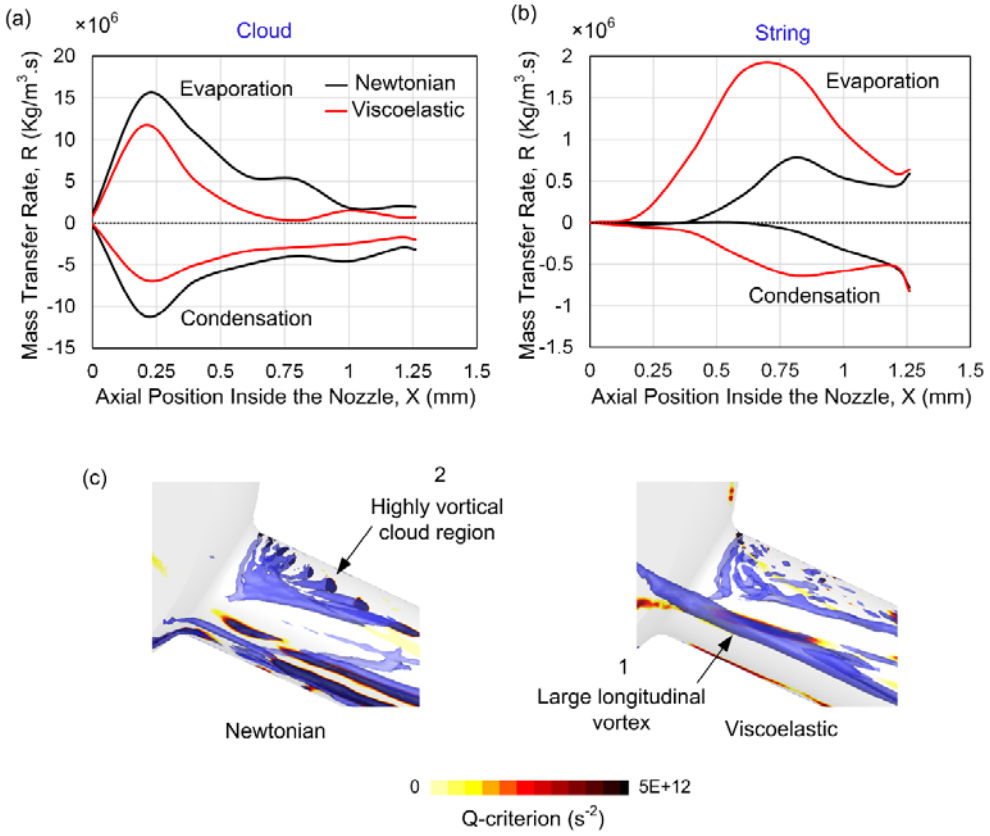

Figure 12. (a) and (b) evaporation and condensations rates computed by the mass transfer rate cavitation model in the cloud and the string cavitation region, (c) vortical flow structures in the vicinity of the injector nozzle entrance plotted using the contours of second invariant of the velocity gradient (Q-criterion) in the nozzle mid-plane and translucent iso-surfaces of Q-criterion at 5E+12 s^{-2}

As it was mentioned earlier, the vortex forming the string cavitation enters the nozzle from the sac volume and is formed by the swirling flow inside the sac volume [70]. Hence the level of turbulence upstream the nozzle entrance, can have a significant effect on the strength of the cavitating vortex. In Figure 13 (a) the flow structures in the sac volume in terms of the second invariant of the velocity gradient are displayed. Circumferential perturbations on the interface of a cavitating vortex can cause strong radial oscillations which result in splitting and collapse of the cavity core[119]. Moreover, flow instabilities upstream the vortex can cause the divergence of the stream tubes forming the vortex core, eventually breaking down the vortex [120]. The turbulent eddies in the sac volume in the Newtonian fluid (Figure 13 (a)) appear to breakdown the coherence of the vortex entering the nozzle. Furthermore, fluid elasticity can suppress

or delay the vortex breakdown as it prevents sharp velocity variations along the vortex centerline which initiate the breakdown process [121].

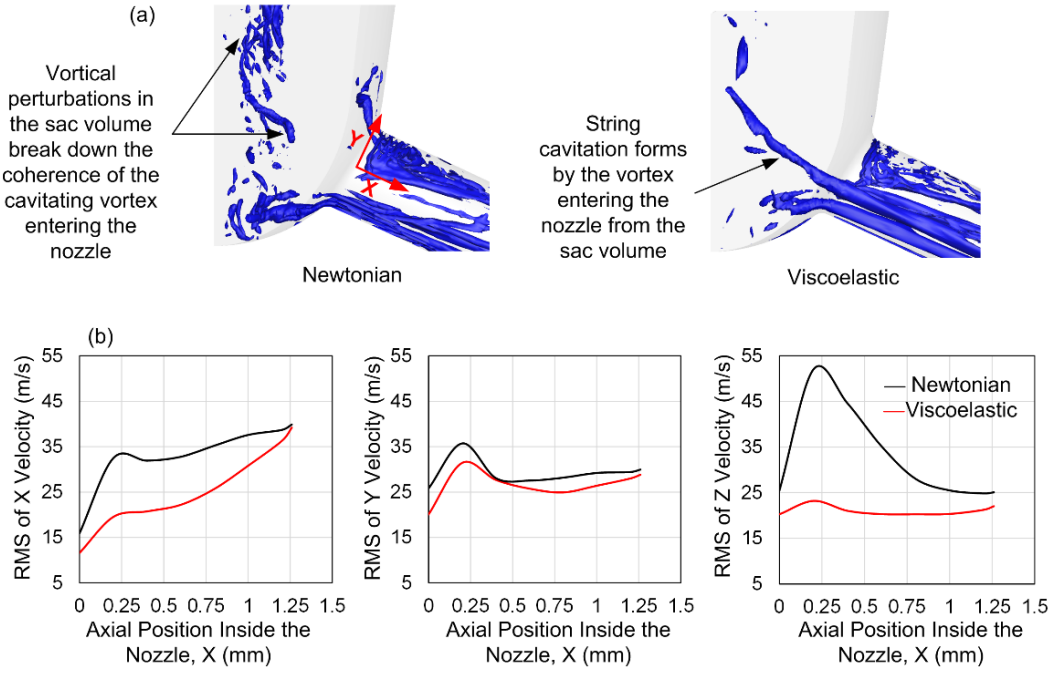

Figure 13. (a) Vortex structures indie the sac volume visualized using the iso-surface of second invariant of the velocity gradient at 4E+12 s^{-2}, (b) velocity fluctuations inside the nozzle plotted in terms of RMS of X,Y and Z velocity, values obtained from surface-averaged data calculated in slices along the nozzle

The vortex disturbance inside the sac volume is significantly lower in the viscoelastic fluid compared to the Newtonian fluid in Figure 13 (a) and the large vortex entering the nozzle can be clearly identified. Reduction of vortex interactions in the sac volume contributes to stabilization of the cavitating vortex upstream of the nozzle entrance, which in turn allows a stronger string cavity to develop inside the nozzle. The fluctuations inside the nozzle in terms of RMS of the velocity components are plotted in Figure 13 (b). It is evident that due to the stabilizing effect of viscoelasticity on flow turbulence, all three components of velocity fluctuations are reduced in the viscoelastic fluid (by 23%, 9% and 31% in X, Y and Z directions respectively). This will therefore reduce the perturbations that destabilize the string cavity coherence inside the nozzle, allowing the cavitation structures to last longer.

4. Conclusions

In this study the effect of viscoelasticity on formation and development of cavitation inside a step nozzle and an injector nozzle is studied in PTT fluids using the Schnerr-Sauer cavitation model and the WALE turbulence model. In the step nozzle, incipient cloud cavitation is forming whereas in the injector the cavitation cloud is fully developed while a string cavitation is forming in the core of the vortex originating from the sac volume.

In the step nozzle case, larger coherent structures become more dominant in the flow as the smaller eddies are suppressed due to flow resistance to rotational motion in the viscoelastic fluid. The dominant frequency of mass flowrate fluctuations is significantly reduced from 168 Hz in the Newtonian fluid to 57 Hz in the viscoelastic fluid and higher frequency (smaller amplitude) fluctuations are damped.

Moreover, fewer cavitating microvortices appear in the viscoelastic fluid and the cavitation cloud structures are altered by viscoelasticity as large-scale cavitating vortices appear stretched and enlarged compared to the Newtonian fluid. Time-averaged statistics show that the vapor volume fraction is reduced more than 50% in the viscoelastic fluid and the cavitation cloud is pushed away from the nozzle wall, while the cloud thickness is reduced by more than 15%.

In the injector test case, the total vapor volume fraction is reduced in the viscoelastic fluid by more than 40%, however there are significant differences in the effect of viscoelasticity on the cloud cavitation and the string cavitation mechanisms. In the cloud cavitation region, viscoelasticity reduces the vapor volume fraction, whereas in the string cavitation region vapor volume fraction is enhanced. String cavitation forms in the core of the quasi-streamwise vortex inside the nozzle and it is prone to breakdown by velocity fluctuations upstream of the nozzle and inside the nozzle. The

cavitating vortex becomes more stable as viscoelasticity stimulates the longitudinal vortices while suppressing the cross-stream fluctuations inside the nozzle and reducing the vortical perturbations in the sac volume. However as vortices in the cloud region rotate out of the cross-sectional plane (vorticity vector positioned in the cross-flow direction), they are damped by viscoelasticity.

Further experimental and numerical investigations on viscoelastic cavitating flows are important for addressing the underlying mechanisms involved in this type of flow. Interface capturing methods and modelling of subgrid scale viscoelastic effects as well as PIV-LIF and X-ray techniques can provide valuable data for understanding the of flow physics and validation of computational studies.

Acknowledgments

This work has received financial support from City, University of London and Lubrizol ltd UK. The authors also acknowledge the contribution of The Lloyd's Register Foundation. Lloyd's Register Foundation helps to protect life and property by supporting engineering-related education, public engagement and the application of research. The authors would also like to thank Dr. Ioannis Karathanassis for the valuable discussions during the preparation of this manuscript.

Competing financial statement:

The authors declare no competing financial interests.

Appendix A: Viscoelastic code validation

Calculations performed with the viscoelastic model are compared against the analytical solution for the fully developed channel flow of the PTT fluid [122]. The tangential and normal components of the stress are calculated for various β values (ratio of solvent to total viscosity) and the relaxation time is chosen such that Deborah number (De = λU/H, where U and H are characteristic velocity and length scales of flow) is equal to 1. Tangential and normal stress components are non-dimensionalized by the stress scale $\mu_p U_N/H$, where H is the channel half-height and U_N is a velocity scale defined as $U_N = -p_z H^2/8\mu_0$ and p_z is the pressure gradient across the channel. The stress values predicted by the code match the analytical calculations.

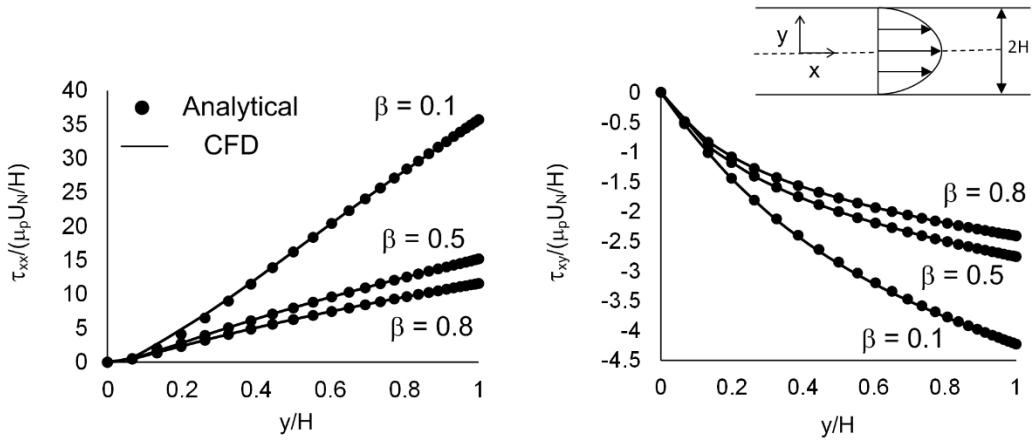

Figure 14. Comparison of the CFD code and the analytical solution for the PTT model, non-dimensionalized normal viscoelastic stresses (left) and tangential viscoelastic stresses (right) in the channel at different viscosity ratios ($\beta = \mu_s / \mu_0$) are compared for ε = 0.25 and De =1

This graph shows that by increasing the polymer strength (lower β values), the stresses are higher in both normal and tangential directions. Moreover in the centerline (y/H = 0), stresses are zero because in the fully developed flow, the velocity gradient approaches zero near the center of the channel. Also as expected, maximum stress values occur at the contact with the wall where the velocity gradient and shear stresses are maximum.

References

1. Tan, D. *et al.* Experimental Investigation of the Role of Large Scale Cavitating Vortical Structures in Performance Breakdown of an Axial Waterjet Pump. *J. Fluids Eng.* **137,** 111301 (2015).

2. Dreyer, M., Decaix, J., Münch‐alligné, C. & Farhat, M. Mind the gap: a new insight into the tip leakage vortex using stereo‐PIV. *Exp Fluids* **55,** 1849 (2014).

3. Arndt, R., Pennings, P., Bosschers, J. & Van Terwisga, T. The singing vortex. *Interface Focus* **5,** 1–11 (2015).

4. Egerer, C. P., Hickel, S., Schmidt, S. J. & Adams, N. A. Large-eddy simulation of turbulent cavitating flow in a micro channel. *Phys. Fluids* **26,** 85102 (2014).

5. Hickel, S. DNS and LES of two-phase flows with cavitation. *Direct Large-Eddy Simul.* **IX,** 595–604 (2015).

6. Koukouvinis, P., Mitroglou, N., Gavaises, M., Lorenzi, M. & Santini, M. Quantitative predictions of cavitation presence and erosion-prone locations in a high-pressure cavitation test rig. *J. Fluid Mech.* **819,** 21–57 (2017).

7. Song, J. H., Johansen, K. & Prentice, P. Covert cavitation: Spectral peak suppression in the acoustic emissions from spatially configured nucleations. *J. Acoust. Soc. Am.* **141,** 216 (2017).

8. Lu, Y., Katz, J. & Prosperetti, A. Dynamics of cavitation clouds within a high-intensity focused ultrasonic beam. *Phys. Fluids* **25,** (2013).

9. Macoskey, J. J. *et al.* Bubble-Induced Color Doppler Feedback Correlates with Histotripsy-Induced Destruction of Structural Components in Liver Tissue. *Ultrasound Med. Biol.* **44,** 602–612 (2018).

10. Bergwerk, W. FLOW PATTERN IN DIESEL NOZZLE SPRAY HOLES. *Proc. Inst. Mech. Eng.* **173,** 655–660 (1959).

11. Schmidt, D. P. & Corradini, M. L. The internal flow of diesel fuel injector nozzles: a review. *Int. J. Engine Res.* **2,** 1–22 (2001).

12. Som, S., Aggarwal, S. K., El-Hannouny, E. M. & Longman, D. E. Investigation of Nozzle Flow and Cavitation Characteristics in a Diesel Injector. *J. Eng. Gas Turbines Power* **132,** 42802 (2010).

13. Duke, D. J., Kastengren, A. L., Tilocco, F. Z., Swantek, A. B. & Powell, C. F. X-RAY RADIOGRAPHY MEASUREMENTS OF CAVITATING NOZZLE FLOW. *At. Sprays* **23,** 841–860 (2013).

14. Giannadakis, E., Gavaises, M. & Arcoumanis, C. Modelling of cavitation in diesel injector nozzles. *J. Fluid Mech.* **616,** 153–193 (2008).

15. Kastengren, A. L. *et al.* TIME-RESOLVED X-RAY RADIOGRAPHY OF SPRAYS FROM ENGINE COMBUSTION NETWORK SPRAY A DIESEL INJECTORS. *At. Sprays* **24,** 251–272 (2014).

16. Mitroglou, N., Lorenzi, M., Santini, M. & Gavaises, M. Application of X-ray micro-computed tomography on high-speed cavitating diesel fuel flows. *Exp. Fluids* **57,** 175 (2016).

17. Örley, F. *et al.* Large-eddy simulation of cavitating nozzle flow and primary jet break-up. *Phys. Fluids* **27,** 86101 (2015).

18. Gopalan, S. & Katz, J. Flow structure and modeling issues in the closure region of attached cavitation. *Phys. Fluids* **12,** 895–911 (2000).

19. Iyer, C. O. & Ceccio, S. L. The influence of developed cavitation on the flow of a turbulent shear layer. *Phys. Fluids* **14,** 3414–3431 (2002).

20. Dittakavi, N., Chunekar, A. & Frankel, S. Large Eddy Simulation of Turbulent-Cavitation Interactions in a Venturi Nozzle. *J. Fluids Eng.* **132,** 121301 (2010).

21. Aeschlimann, V., Barre, S. & Djeridi, H. Velocity field analysis in an experimental cavitating mixing layer. *Phys. Fluids* **23,** 55105 (2011).

22. Ganesh, H., Makiharju, S., Ceccio, S. & Ganesh, H. Bubbly shock propagation as a mechanism for sheet-to-cloud transition of partial cavities. *J. Fluid Mech* **802,** 37–78 (2016).

23. Karathanassis, I. K. *et al.* High-speed visualization of vortical cavitation using synchrotron radiation. *J. Fluid Mech* **838,** 148–164 (2018).

24. Sridhar, G. & Katz, J. Effect of entrained bubbles on the structure of vortex rings. *J. Fluid Mech.* **397,** 171–202 (1999).

25. Ceccio, S. L. Friction Drag Reduction of External Flows with Bubble and Gas Injection. *Annu. Rev. Fluid Mech* **42,** 183–203 (2010).

26. Ferrante, A. & Elghobashi, S. Reynolds number effect on drag reduction in a microbubble-laden spatially developing turbulent boundary layer. *J. Fluid Mech* **543,** 93–106 (2005).

27. Sugiyama, K., Calzavarini, E. & Lohse, D. Microbubbly drag reduction in Taylor-Couette flow in the wavy vortex regime. *J. Fluid Mech.* **608,** 21–41 (2008).

28. Kawakami, E. & Arndt, R. E. A. Investigation of the Behavior of Ventilated Supercavities. *J. Fluids Eng.* **133,** 91305 (2011).

29. Karn, A. *et al.* An experimental investigation into supercavity closure mechanisms. *J. Fluid Mech* **789,** 259–284 (2016).

30. Mäkiharju, S. A., Ganesh, H. & Ceccio, S. L. The dynamics of partial cavity formation, shedding and the influence of dissolved and injected non-condensable gas. *J. Fluid Mech* **829,** 420–458 (2017).

31. Legner, H. H. A simple model for gas bubble drag reduction. *Phys. Fluids* **27,** 2788 (1984).

32. Llewellin, E. W. *et al.* The Rheology of a Bubbly Liquid. *Source Proc. Math. Phys. Eng. Sci.* **458,** 987–1016 (2001).

33. Toms, B. A. Some observations on the flow of linear polymer solutions through straight tubes at large Reynolds numbers. in *Proceedings of the 1st International Congress on Rheology* (1948).

34. Virk, P. S. An elastic sublayer model for drag reduction by dilute solutions of linear macromolecules. *J. Fluid Mech.* **45,** 417–440 (1971).

35. Virk, P. S. Drag reduction fundamentals. *AIChE J.* **21,** 625–656 (1975).

36. Ohlendorf, D., Interthal, W. & Hoffmann, H. Surfactant systems for drag reduction: Physico-chemical properties and rheological behaviour. *Rheol. Acta* **25,** 468–486 (1986).

37. Bewersdorff, H.-W. & Ohlendon, D. The behaviour of drag-reducing cationic surfactant solutions. *Colloid Polym. Sci.* **266,** 941–953 (1988).

38. Luchik, T. S. & Tiederman, W. G. Turbulent structure in low-concentration drag-reducing channel flows. *J. Fluid Mech.* **190,** 241–263 (1988).

39. Dimitropoulos, C. D., Sureshkumar, R. & Beris, A. N. Direct numerical simulation of viscoelastic turbulent channel flow exhibiting drag reduction: effect of the variation of rheological parameters. *J. Nonnewton. Fluid Mech.* **79,** 433–468 (1998).

40. Li, F.-C., Kawaguchi, Y. & Hishida, K. Investigation on the characteristics of turbulence transport for momentum and heat in a drag - reducing surfactant solution flow. *Phys. Fluids* **16,** 3281–3295 (2004).

41. Dimitropoulos, C. D., Dubief, Y., Shaqfeh, E. S. G., Moin, P. & Lele, S. K. Direct numerical simulation of polymer-induced drag reduction in turbulent boundary layer flow. *Phys. Fluids* **17,** 11705 (2005).

42. Dubief, Y. *et al.* On the coherent drag-reducing and turbulence-enhancing behaviour of polymers in wall flows. *J. Fluid Mech.* **514,** 271–280 (2004).

43. White, C. M. & Mungal, M. G. Mechanics and prediction of turbulent drag reduction with polymer additives. *Annu. Rev. Fluid Mech.* **40,** 235–256 (2008).

44. Procaccia, I., L'vov, V. S. & Benzi, R. Colloquium: Theory of drag reduction by polymers in wall-bounded turbulence. *Rev. Mod. Phys.* **80,** 225–247 (2008).

45. Xi, L. & Graham, M. Turbulent drag reduction and multistage transitions in viscoelastic minimal flow units. *J. Fluid Mech.* **647,** 421–452 (2010).

46. Graham, M. D. Drag reduction and the dynamics of turbulence in simple and complex fluids. *Phys. Fluids* **26,** 101301–24 (2014).

47. Japper-Jaafar, A., Escudier, M. P. & Poole, R. J. Laminar, transitional and turbulent annular flow of drag-reducing polymer solutions. *J. Non-Newtonian Fluid Mech* **165,** 1357–1372 (2010).

48. Owolabi, B. E., Dennis, D. J. C. & Poole, R. J. Turbulent drag reduction by polymer additives in parallel-shear flows. *J. Fluid Mech* **827,** R4 (2017).

49. Li, C.-F., Sureshkumar, R. & Khomami, B. Influence of rheological parameters on polymer induced turbulent drag reduction. *J. Nonnewton. Fluid Mech.* **140,** 23–40 (2006).

50. Rose, G. D. & Foster, K. L. Drag reduction and rheological properties of cationic viscoelastic surfactant formulationsS. *J. Nonnewton. Fluid Mech.* **31,** 59–85 (1989).

51. Zakin, J. L., Lu, B. & Bewersdorff, H.-W. Surfactant drag reduction. *Rev. Chem. Eng.* **14,** 253–320 (1998).

52. *Wormlike Micelles: Advances in Systems, Characterisation and Applications*. (Royal Society of Chemistry, 2017). doi:10.1039/9781782629788

53. Lumley, J. L. Drag reduction in turbulent flow by polymer additives. *J. Polym. Sci. Macromol. Rev.* **7,** 263–290 (1973).

54. Ryskin, G. Turbulent Drag Reduction by Polymers: A Quantitative Theory. *Phys. Rev. Lett.* **59,** 2059–2062 (1987).

55. L 'vov, V. S., Pomyalov, A., Procaccia, I. & Tiberkevich, V. Drag Reduction by Polymers in Wall Bounded Turbulence. *Phys. Rev. Lett.* **92,** 244503 (2004).

914 56. Tabor, M. & de Gennes, P. G. A Cascade Theory of Drag Reduction. *Europhys. Lett.* **2,**
915 519–522 (1986).

916 57. Goldberg, B. B., Liu, J.-B. & Forsberg, F. ULTRASOUND CONTRAST AGENTS: A
917 REVIEW. *Ultrasound Med. Biol* **20,** 319–333 (1994).

918 58. Roberts, W. W. *et al.* Pulsed Cavitational Ultrasound: A Noninvasive Technology for
919 Controlled Tissue Ablation (Histotripsy) in the Rabbit Kidney. *J. Urol.* **175,** 734–738
920 (2006).

921 59. Brujan, E. A., Ohl, C. D., Lauterborn, W. & Philipp, A. Dynamics of laser-induced
922 cavitation bubbles in polymer solutions. *Acta Acust. united with Acust.* **82,** 423–430
923 (1996).

924 60. Chahine, G. L. & Fruman, D. H. Dilute polymer solution effects on bubble growth and
925 collapse. *Phys. Fluids* **22,** 1406 (1979).

926 61. Brujan, E. A., Ikeda, T. & Matsumoto, Y. Dynamics of ultrasound - induced cavitation
927 bubbles in non - Newtonian liquids and near a rigid boundary. *Phys. Fluids* **16,** 2402–
928 2410 (2004).

929 62. Lind, S. J. & Phillips, T. N. The influence of viscoelasticity on the collapse of cavitation
930 bubbles near a rigid boundary. *Theor. Comput. Fluid Dyn.* **26,** 245–277 (2012).

931 63. Lind, S. J. & Phillips, T. N. Bubble Collapse in Compressible Fluids using a Spectral
932 Element Marker Particle Method. Part 2. Viscoelastic Fluids. *Int. J. Numer. Meth. Fluids*
933 **71,** 1103–1130 (2013).

934 64. Brujan, E.-A. Shock wave emission from laser-induced cavitation bubbles in polymer
935 solutions. *Ultrasonics* **48,** 423–426 (2008).

936 65. Hua, C. & Johnsen, E. Nonlinear oscillations following the Rayleigh collapse of a gas
937 bubble in a linear viscoelastic (tissue-like) medium. *Phys. Fluids* **25,** 83101 (2013).

938 66. Warnez, M. T. & Johnsen, E. Numerical modeling of bubble dynamics in viscoelastic
939 media with relaxation. *Phys. Fluids* **27,** 63103 (2015).

67. Jiménez-Fernández, J. & Crespo, A. Bubble oscillation and inertial cavitation in viscoelastic fluids. *Ultrasonics* **43,** 643–651 (2005).

68. Brennen, C. E. *Cavitation and Bubble Dynamics*. (Cambridge University Press, 2013).

69. Andriotis, A., Gavaises, M. & Arcoumanis, C. Vortex flow and cavitation in diesel injector nozzles. *J. Fluid Mech.* **610,** 195–215 (2008).

70. Gavaises, M., Andriotis, A., Papoulias, D., Mitroglou, N. & Theodorakakos, A. Characterization of string cavitation in large-scale Diesel nozzles with tapered holes. *Phys. Fluids* **21,** 52107–52107 (2009).

71. Callenaere, M., Franc, J., Michel, J. & Riondet, M. The cavitation instability induced by the development of a re-entrant jet. *J. Fluid Mech* **444,** 223–256 (2001).

72. Chahine, G. L., Frederick, G. F. & Bateman, R. D. Propeller Tip Vortex Cavitation Suppression Using Selective Polymer Injection. *J. Fluids Eng.* **115,** 497–503 (1993).

73. Chang, N., Ganesh, H., Yakushiji, R. & Ceccio, S. L. Tip Vortex Cavitation Suppression by Active Mass Injection. *J. Fluids Eng.* **133,** 111301 (2011).

74. Thien, N. P. & Tanner, R. I. A new constitutive equation derived from network theory. *J. Nonnewton. Fluid Mech.* **2,** 353–365 (1977).

75. Poole, R. J., Escudier, M. P., Afonso, A. & Pinho, F. T. Laminar flow of a viscoelastic shear-thinning liquid over a backward-facing step preceded by a gradual contraction. *Phys. Fluids* **19,** 1–17 (2007).

76. Afonso, A. & Pinho, F. T. Numerical investigation of the velocity overshoots in the flow of viscoelastic fluids inside a smooth contraction. *J. Nonnewton. Fluid Mech.* **139,** 1–20 (2006).

77. Nicoud, F. & Ducros, F. Subgrid-scale stress modelling based on the square of the velocity gradient tensor. *Flow, Turbul. Combust.* **62,** 183–200 (1999).

78. Schnerr, G. H. & Sauer, J. Physical and numerical modeling of unsteady cavitation

965 dynamics. in *Fourth International Conference on Multiphase Flow* (2001).

966 79. Franc, J.-P. & Michel, J.-M. *Fundamentals of Cavitation*. (Springer Netherlands, 2005).
967 doi:10.1007/1-4020-2233-6

968 80. Sibley, D. N. Viscoelastic Flows of PTT Fluids. (University of Bath, 2010).

969 81. Jasak, H., Weller, H. G. & Gosman, A. A. D. HIGH RESOLUTION NVD DIFFERENCING
970 SCHEME FOR ARBITRARILY UNSTRUCTURED MESHES. *Int. J. Numer. Meth. Fluids*
971 **31,** 431–449 (1999).

972 82. Sureshkumar, R. & Beris, A. N. Effect of artificial stress diffusivity on the stability of
973 numerical calculations and the flow dynamics of time-dependent viscoelastic flows. *J.*
974 *Nonnewton. Fluid Mech.* **60,** 53–80 (1995).

975 83. Issa, R. I. Solution of the Implicitly Discretised Fluid Flow Equations by Operator-
976 Splitting. *J. Comput. Phys.* **62,** 40–65 (1985).

977 84. Chen, Z. J. & Przekwas, A. J. A coupled pressure-based computational method for
978 incompressible/compressible flows. *J. Comput. Phys.* **229,** 9150–9165 (2010).

979 85. Giudice, F. Del, Haward, S. J. & Shen, A. Q. Relaxation time of dilute polymer solutions:
980 A microfluidic approach. *J. Rheol. (N. Y. N. Y).* **61,** 327–337 (2017).

981 86. Valente, P. C., Da Silva, C. B. & Pinho, F. T. The effect of viscoelasticity on the turbulent
982 kinetic energy cascade. *J . Fluid Mech* **760,** 39–62 (2014).

983 87. Yu, B., Li, F. & Kawaguchi, Y. Numerical and experimental investigation of turbulent
984 characteristics in a drag-reducing flow with surfactant additives. *Int. J. heat fluid flow* **25,**
985 961–974 (2004).

986 88. Sou, A., Biçer, B. & Tomiyama, A. Numerical simulation of incipient cavitation flow in a
987 nozzle of fuel injector. *Comput. Fluids* **103,** 42–48 (2014).

988 89. Koukouvinis, Naseri, H. & Gavaises, M. Performance of turbulence and cavitation
989 models in prediction of incipient and developed cavitation. *Int. J. Engine Res.* **18,** 333–

350 (2016).

90. Addad, Y., Gaitonde, U., Laurence, D. & Rolfo, S. in *In: J. Meyers, B.J. Geurts, P. Sagaut (eds) Quality and Reliability of Large-Eddy Simulations. Ercoftac Series* **12,** 93–103 (Springer, Dordrecht, 2008).

91. Howard, R. J. A. & Pourquie, M. Large eddy simulation of an Ahmed reference model. *J. Turbul.* **3,** (2002).

92. Lesieur, M., Métais, O. & Comte, P. *Large-eddy simulations of turbulence*. (Cambridge University Press, 2005).

93. Lesieur, M. *Turbulence in Fluids*. (Springer Science & Business Media, 2012).

94. Tennekes, H. & Lumley, J. L. *A first course in turbulence*. (MIT Press, 1972).

95. Örley, F., Hickel, S., Schmidt, S. J. & Adams, N. A. Large-Eddy Simulation of turbulent, cavitating fuel flow inside a 9-hole Diesel injector including needle movement. *Int. J. Engine Res.* **18,** 195–211 (2017).

96. Kolev, N. I. *Multiphase Flow Dynamics*. (Springer, 2005).

97. Richter, D., Iaccarino, G. & Shaqfeh, E. S. G. Effects of viscoelasticity in the high Reynolds number cylinder wake. *J. Fluid Mech.* **693,** 297–318 (2012).

98. Haller, G. An objective definition of a vortex. *J. Fluid Mech.* **525,** 1–26 (2005).

99. Cadot, O. & Lebey, M. Shear instability inhibition in a cylinder wake by local injection of a viscoelastic fluid. *Phys. Fluids* **11,** 494–496 (1999).

100. Lin, J., Yu, Z. & Shao, X. Coherent structures in the mixing layers of a non-Newtonian fluid. *J. Turbul.* **5,** 39 (2004).

101. Pereira, A. S., Mompean, G., Thais, L. & Soares, E. J. Transient aspects of drag reducing plane Couette flows. *J. Nonnewton. Fluid Mech.* **241,** 60–69 (2017).

102. Pereira, A. S., Mompean, G., Thais, L. & Thompson, R. L. Statistics and tensor analysis of polymer coil-stretch mechanism in turbulent drag reducing channel flow. *J. Fluid*

Mech. **824,** 135–173 (2017).

103. Seyer, F. A. & Metzner, A. B. Turbulence phenomena in drag reducing systems. *AIChE J.* **15,** 426–434 (1969).

104. Housiadas, K. D. & Beris, A. N. Direct numerical simulations of viscoelastic turbulent channel flows at high drag reduction. *Korea - Aust. Rheol. J.* **17,** 131–140 (2005).

105. Xie, Y.-C. *et al.* Effects of polymer additives in the bulk of turbulent thermal convection. *J . Fluid Mech* **784,** R3 (2015).

106. Valente, P. C., da Silva, C. B. & Pinho, F. T. Energy spectra in elasto-inertial turbulence. *Phys. Fluids* **28,** 75108 (2016).

107. Soldati, A. & Banerjee, S. Turbulence modification by large-scale organized electrohydrodynamic flows. *Phys. Fluids* **10,** 1742–1756 (1998).

108. Pelz, P. F. *et al.* in *Advanced Experimental and Numerical Techniques for Cavitation Erosion Prediction* (eds. Kim K., Chahine G., Franc J. P. & Karimi A.) (2014). doi:10.1007/978-94-017-8539

109. Hegedús, F., Hós, C., Pandula, Z. & Kullmann, L. Measurement on the cavitating vortex shedding behind rectangular obstacles. *IOP Conf. Ser. Earth Environ. Sci.* **12,** 12066 (2010).

110. Kim, B. K. & Telionis, D. P. The effect of polymer additives on laminar separation. *Phys. Fluids A Fluid Dyn.* **1,** 267–273 (1989).

111. Oliveira, P. J. Method for time-dependent simulations of viscoelastic flows: vortex shedding behind cylinder. *J. Nonnewton. Fluid Mech.* **101,** 113–137 (2001).

112. Norouzi, M., Varedi, S. R. & Zamani, M. Wake instability of viscoelastic flows past an unconfined inclined square cylinder. *Phys. Fluids* **28,** 23101 (2016).

113. Sureskumar, R., Beris, A. N. & Handler, A. H. Direct numerical simulation of the turbulent channel flow of a polymer solution. *Phys. Fluids* **9,** 743–755 (1997).

114. Afzal, H., Arcoumanis, C., Gavaises, M. & Kampanis, N. Internal flow in diesel injector nozzles: modelling and experiments. *IMechE Pap. S* 25–44 (1999).

115. Duke, D. *et al.* X-ray imaging of cavitation in Diesel injectors. *SAE Int. J. Engines* **7,** 1003–1016 (2014).

116. DEGANI, D., SEGINER, A. & LEVY, Y. Graphical visualization of vortical flows by means of helicity. *AIAA J.* **28,** 1347–1352 (1990).

117. Tsukahara, T., Motozawa, M. & Tsurumi, D. PIV and DNS analyses of viscoelastic turbulent flows behind a rectangular orifice. *Int. J. Heat Fluid Flow* 66–79 (2013).

118. Kim, K., Adrian, R. J., Balachandar, S. & Sureshkumar, R. Dynamics of Hairpin Vortices and Polymer-Induced Turbulent Drag Reduction. *Phys. Rev. Lett.* **100,** 134504 (2008).

119. Choi, J., Hsaio, C., Chahine, G. & Ceccio, S. Growth, oscillation and collapse of vortex cavitation bubbles. *J. Fluid Mech.* **624,** 255–279 (2009).

120. Hall, M. G. VORTEX BREAKDOWN. *Annu. Rev. Fluid Mech.* **4,** 195–318 (1972).

121. Stokes, J. R., W Graham, L. J., Lawson, N. J. & Boger, D. V. Swirling flow of viscoelastic fluids. Part 1. Interaction between inertia and elasticity. *J. Fluid Mech* **429,** 67–115 (2001).

122. Cruz, D. O. A., Pinho, F. T. & Oliveira, P. J. Analytical solutions for fully developed laminar flow of some viscoelastic liquids with a Newtonian solvent contribution. *J. Nonnewton. Fluid Mech.* **132,** 28–35 (2005).